

Autophagosome formation is initiated at phosphatidylinositol synthase-enriched ER subdomains

Taki Nishimura^{1,5*}, Norito Tamura^{1,2}, Nozomu Kono³, Yuta Shimanaka³, Hiroyuki Arai^{3,4}, Hayashi Yamamoto¹ and Noboru Mizushima^{1*}

¹ Department of Biochemistry and Molecular Biology, Graduate School and Faculty of Medicine, The University of Tokyo, Tokyo 113-0033, Japan

² Department of Developmental and Regenerative Biology, Medical Research Institute, Tokyo Medical and Dental University, Tokyo 113-8519, Japan

³ Department of Health Chemistry, Graduate School of Pharmaceutical Sciences, The University of Tokyo, Tokyo 113-0033, Japan

⁴ AMED-CREST, Japan Agency for Medical Research and Development, Tokyo 100-0004, Japan

⁵ Present address: Medical Research Council Laboratory for Molecular Cell Biology, University College London, London WC1E 6BT, UK

*Correspondence should be addressed to:

Taki Nishimura

Telephone: +44-020-7679-7208

E-mail: t.nishimura@ucl.ac.uk

Noboru Mizushima

Telephone: +81-3-5841-3440

FAX: +81-3-3815-1490

E-mail: nmizu@m.u-tokyo.ac.jp

Running Title: PIS-enriched ER subdomains in autophagy (39 characters/Max 40 characters)

Total number of characters: 53,655 characters/Max 55,000 characters

ABSTRACT

The autophagosome, a double-membrane structure mediating degradation of cytoplasmic materials by macroautophagy, is formed in close proximity to the endoplasmic reticulum (ER). However, how the ER membrane is involved in autophagy initiation and to which membrane structures the autophagy-initiation complex is localized have not been fully characterized. Here, we were able to biochemically analyze autophagic intermediate membranes and show that the autophagy-initiation complex containing ULK and FIP200 first associates with the ER membrane. To further characterize the ER subdomain, we screened phospholipid biosynthetic enzymes and found that the autophagy-initiation complex localizes to phosphatidylinositol synthase (PIS)-enriched ER subdomains. Then, the initiation complex translocates to the ATG9A-positive autophagosome precursors in a PI3P-dependent manner. Depletion of phosphatidylinositol (PI) by targeting bacterial PI-specific phospholipase C to the PIS domain impairs recruitment of downstream autophagy factors and autophagosome formation. These findings suggest that the autophagy-initiation complex, the PIS-enriched ER subdomain, and ATG9A vesicles together initiate autophagosome formation.

(152 words/Max 175 words)

Key words: ATG9A/Autophagy/FIP200/Phosphatidylinositol synthase/The ULK complex

INTRODUCTION

Macroautophagy (hereafter referred to as autophagy) is a catabolic process that is highly conserved among eukaryotes. When autophagy is induced, a part of the cytoplasm is surrounded by a membrane sac, termed the isolation membrane (also known as the phagophore). The isolation membrane expands to form a double-membrane autophagosome, which subsequently fuses with lysosomes for degradation of engulfed materials. Autophagosome formation involves a number of autophagy-related (ATG) proteins (Xie & Klionsky, 2007; Mizushima et al, 2011). Systematic hierarchical analysis revealed that the serine/threonine kinase Atg1 (UNC-51-like kinases (ULKs) in mammals) complex is the most upstream unit among the ATG proteins (Suzuki et al, 2007; Itakura & Mizushima, 2010). This complex is composed of Atg1, Atg13, Atg17, Atg29, and Atg31 in yeast and ULK1 (or ULK2), ATG13, FIP200 (also known as RB1CC1 and partially homologous to yeast Atg11 and Atg17), and ATG101 in mammals (Mizushima et al, 2011). Atg17 and FIP200 are proposed to act as a scaffold for recruitment of downstream Atg proteins (Ragusa et al, 2012; Suzuki et al, 2013). Upon nutrient deprivation, Atg1/ULK is activated and phosphorylates downstream effectors, such as BECLIN1 (Russell et al, 2013), ATG14 (Park et al, 2016), and Atg9/ATG9A (Papinski et al, 2014; Zhou et al, 2017), to induce autophagosome formation. Thus, it is critical to understand the membrane structures/domains on which the activated Atg1/ULK complex acts. It is well known that early autophagic structures are formed in close apposition to the endoplasmic reticulum (ER)-related subdomains such as the omegasome (Axe et al, 2008), ER-mitochondrial contact site (Hamasaki et al, 2013), ER exit site (Graef et al, 2013; Suzuki et al, 2013), ER-Golgi intermediate compartment (ERGIC) (Ge et al, 2013), and isolation membrane-associated tubular/vesicular structures (Uemura et al, 2014). In mammalian cells, the ULK complex is translocated to punctate structures in tight association with the ER by both phosphatidylinositol (PI)3P-dependent and -independent mechanisms (Itakura & Mizushima, 2010; Karanasios et al, 2013). It was also reported that the ULK complex localizes to transferrin receptor-positive recycling endosomes (Longatti et al, 2012). However, the precise target membrane of the Atg1/ULK complex remains unknown.

Here, we performed systematic biochemical analysis using various ATG knockout cells and found that the ULK complex first localizes to PI synthase (PIS)-enriched ER subdomains and then translocates to the ATG9A-positive autophagosome precursors in a PI3P-dependent manner. PI in the PIS-enriched membrane is required for autophagosome formation.

RESULTS

The autophagy-initiation complex associates with two distinct membrane structures

To analyze the autophagic membranes, cell homogenates of mouse embryonic fibroblasts (MEFs) were subjected to flotation analysis. As for wild-type (WT) MEF homogenates, ATG proteins, except for the membrane protein ATG9A and membrane-bound microtubule-associated protein light chain 3 (LC3)-II, mostly remained in the bottom cytosolic fractions (Fig 1A). Consistent with a previous report (Chan et al, 2009), small proportions of the ULK complex components were found in floated membrane fractions under growing conditions. Flotation of FIP200, ATG13, ATG101, and WIPI2 into lighter-density fractions became clearer under starvation condition (Fig EV1A), indicating that autophagic membranes were floated. In order to enrich these autophagic membranes, we used several ATG-deficient cell lines, in which autophagosome formation is blocked at various steps leading to accumulation of autophagic intermediate structures at specific stages under growing conditions (Fig EV1B) (Itakura & Mizushima, 2010; Kageyama et al, 2011; Kishi-Itakura et al, 2014).

We first analyzed homogenates obtained from ATG14 knockout (KO) and ATG3 KO MEFs. ATG14, a component of the PI 3-kinase complex, and ATG3 are required for the nucleation step and the elongation or closure step during autophagosome formation, respectively (Fig 1B) (Mizushima et al, 2011; Kishi-Itakura et al, 2014). Thus, early autophagosome precursors and elongating isolation membranes accumulate in ATG14 KO and ATG3 KO cells, respectively. As for the ATG14 KO homogenate, in addition to ATG9A and LC3-II, the ULK complex components (FIP200, ATG13, ATG101, and ULK1) were floated into middle-density fractions (Fractions 5 to 7) even under growing conditions (Fig 1C, *). On the other hand, the isolation membrane-resident proteins WIPI2 and ATG5 were not clearly floated. These results suggest that these middle-density fractions contain autophagic precursor membranes, to which the ULK complex is recruited in a PI 3-kinase-independent manner. Similarly, when ATG3 KO homogenates were used, the ULK complex components and autophagy-specific PI 3-kinase complex components (ATG14, VPS34, and BECLIN1) were floated into the middle-density fractions (Fractions 4 to 7) (Fig 1D, **). In contrast to ATG14 KO

homogenates, the ULK complex components, WIPI2, and ATG5 were also enriched in the top (lightest) fraction (Fraction 1) in ATG3 KO homogenates (Fig 1D, ***), suggesting that the top fraction contains elongating isolation membranes. To confirm whether the flotation of these ATG proteins was dependent on formation of the isolation membrane, the effect of acute inhibition of the PI 3-kinase, which is required for isolation membrane elongation (Kishi-Itakura et al, 2014), was examined using wortmannin. The amounts of the ULK complex components, WIPI2, and ATG5 in the top fraction were markedly reduced in ATG3 KO cells after wortmannin treatment (Fig 1E and F), suggesting that isolation membranes are indeed enriched in the top fraction. On the other hand, the flotation of the ULK complex components into the middle-density fractions was unaffected by wortmannin treatment (Fig 1F), which is consistent with the results in ATG14 KO cells (Fig 1C). While the puncta of WIPI2, a PI3P-binding protein, were sensitive to wortmannin, a significant proportion of the FIP200 puncta was not (Fig EV1H). These results suggest that the ULK complex is sequentially recruited to the two distinct membrane structures with middle and light densities in PI3P-independent and -dependent manners, respectively. These structures can be separated using ATG14 KO and ATG3 KO cells.

FIP200 tethers the ULK complex subunits to membranes

Next, we examined which component of the ULK complex determines its membrane targeting. In FIP200 KO cells, ATG13, ATG101, and ULK1 were not clearly floated into the middle-density fractions (Fig EV1C). By contrast, FIP200 was floated in all of the ULK1/2 double KO (DKO), ATG13 KO, and ATG101 KO cells (Fig EV1D-F). ATG101 and ULK1 were not clearly floated in ATG13 KO cells (Fig EV1E). Consistently, FIP200 localized to punctate structures in ATG13 KO, ATG101 KO, and ULK1/2 DKO MEFs (Fig EV1G). These results suggest that FIP200 has the ability to target membranes independently of the other components of the ULK complex.

FIP200 is co-purified with the ER-related membranes and ATG9A-positive isolation membranes

Our flotation analysis demonstrated that a significant population of the ATG9A-positive membranes was also collected in the middle- and light-density fractions, in which the ULK complex components accumulated when autophagosome formation was blocked (Fig 1C and D, asterisks). In mammals, it has been reported that ATG9A dynamically

associates with the isolation membrane, but is not contained in the isolation membrane or autophagosomal membranes (Orsi et al, 2012; Lamb et al, 2016). On the other hand, in yeast, Atg9-containing vesicles are thought to be a seed membrane for autophagosome biogenesis and Atg9 is indeed incorporated into autophagic membranes (Yamamoto et al, 2012). These findings prompted us to investigate the relationship between the ULK complex and ATG9A vesicles in these fractions. When ATG9A vesicles were purified from the middle-density fractions derived from non-starved WT (Fig EV2A) and ATG14 KO MEF homogenates (Fig EV2B), RAB1A (a mammalian Ypt1 homolog) was co-precipitated (Fig 2A-C). This is consistent with previous reports that Ypt1 is recruited to Atg9 vesicles in yeast (Kakuta et al, 2012). However, FIP200 was not detected in these FLAG-ATG9A immunoprecipitates from the middle-density fractions of WT or ATG14 KO MEFs (Fig 2B and C), although both ATG9A and FIP200 were present in these fractions in ATG14 KO MEFs (Fig EV2B). These data suggest that FIP200 is mainly recruited to membrane structures other than ATG9A vesicles in ATG14 KO MEFs. In line with this, FIP200 was clearly floated to the middle-density fractions in the absence of ATG9A (Fig EV2C). Furthermore, FIP200 formed punctate structures in ATG9A KO MEFs (Fig EV1G), as did ULK1 (Itakura et al, 2012; Orsi et al, 2012). These results suggest that the ULK complex can target some membrane structures other than ATG9A vesicles at an early step during autophagosome formation. We further found that the middle-density fractions contained the ER membranes and, in these fractions of ATG14 KO homogenates, FIP200 was co-precipitated with ER membranes purified with FLAG-tagged SEC61B (Fig 2D). These results suggest that the ULK complex localizes to the ER-related membrane in the absence of autophagy-specific PI 3-kinase.

Although FIP200 and ATG9A were not co-purified in the middle-density fractions of ATG14 KO homogenate, FIP200 and WIPI2, another isolation membrane protein, were co-purified with FLAG-ATG9A from the top fraction of ATG3 KO homogenates (Fig 3A). These results suggest that FIP200 resides on isolation membranes together with ATG9A in ATG3 KO MEFs. In contrast to ATG14 KO homogenates (Fig 2C), small amounts of FIP200 and WIPI2 were co-precipitated with FLAG-ATG9A from the middle-density fractions of ATG3 KO homogenates (Fig 3B). Similarly, SEC61B and GFP-ATG14 were co-precipitated with FLAG-ATG9A in these middle fractions (Fig 3B and C). SEC61B was co-precipitated with FLAG-ATG9A from the middle-density fractions of ATG3 KO homogenates more efficiently than from those of WT or ATG14 KO homogenates (Fig 2B and C). These data suggest that ATG9A-containing

autophagosome precursor membranes are associated with the ER in ATG3 KO cells. Overall, we conclude that FIP200 can be recruited to two different membranes: the ER-related membrane (ATG14 KO, Fractions 4-7) and the isolation membrane (ATG3 KO, Fraction 1) (Fig 3D). The co-purification of ATG9A, FIP200, WIPI2, ATG14, and SEC61B from the middle-density fractions of ATG3 KO homogenates would reflect the ER-isolation membrane contact (ATG3 KO, Fractions 4-7) (Fig 3D).

FIP200 is recruited to the PIS-enriched ER subdomain at the initiation stage

In spite of the fact that FIP200 associates with the ER membrane at an early stage of autophagy, it does not show an ER-like reticular pattern but a punctate distribution. This led us to hypothesize that FIP200 might be recruited to an ER subdomain. The ER is known to be the major site of cellular phospholipid synthesis, which would be required for autophagosome biogenesis. Recent studies have demonstrated that several phospholipid-metabolizing enzymes are segregated on the ER membrane (English & Voeltz, 2013; Pol et al, 2014). To characterize the ER subdomain that associates with FIP200, we screened phospholipid biosynthetic enzymes involved in the *de novo* synthesis and remodeling pathways that colocalized with FIP200 (Fig 4A) (Shindou & Shimizu, 2009; Pol et al, 2014). To facilitate the accumulation of FIP200 at the ER subdomain, cells were treated with wortmannin. We found that phosphatidylinositol synthase (PIS), cholinephosphotransferase 1 (CPT1), choline/ethanolaminephosphotransferase 1 (CEPT1), phosphatidylserine synthase 1 (PSS1), and phospholipase D1A (PLD1A) were colocalized with FIP200 in these wortmannin-treated cells under starvation conditions (Fig 4B). Among these enzymes identified, we focused on PIS because this enzyme catalyzes the formation of PI, which is a precursor of PI3P required for autophagosome formation (Kihara et al, 2001). It was reported that PIS localizes to unique compartments: PIS is located in a highly dynamic ER-related compartment (Kim et al, 2011) and leading edges of ER tubules (English & Voeltz, 2013). When autophagosome formation was blocked at an early stage by wortmannin treatment, more than 70% of the FIP200 puncta were colocalized with PIS-GFP (Fig 5A and B), suggesting that FIP200 is recruited to PIS puncta at an early stage. PIS-GFP was not degraded in response to starvation unlike p62, a typical autophagy substrate (Fig EV3), ruling out the possibility that PIS accumulates as an autophagic substrate. In these wortmannin-treated starved cells, PIS and FIP200 double-positive puncta did not colocalize with the ER exit site marker SEC31A or mitochondria (Fig 5C and D). Furthermore, clearly separated PIS structures did not

colocalize with ERGIC53 under wortmannin-treated conditions (Fig EV4). These results suggest that the PIS puncta are distinct from the ERGIC, ER exit site, and ER-mitochondrial contact site. The colocalization of PIS and FIP200 was also observed in ATG14 KO MEFs, in which early autophagic structures accumulated (Fig 5A). Also, we observed biochemically that FIP200 associated with PIS-enriched membranes purified from ATG14 KO MEFs (Fig 5E). This association disappeared in the presence of detergent, suggesting that the FIP200 co-precipitation was not simply caused by non-physiological aggregation but in a membrane-dependent manner. Moreover, in line with our model (Fig 3D; ATG14 KO, Fractions 4-7), co-precipitation of ATG9A with PIS-enriched membranes was not observed (Fig 5E). Overall, we conclude that FIP200 is recruited to the PIS-enriched ER subdomain at an early stage of autophagy, upstream of the action of PI 3-kinase.

The ULK complex forms a punctate structure on PIS-positive membranes

To further characterize the localization of FIP200, we used a super-resolution structured illumination microscope (SR-SIM), which has ~120-nm lateral resolution. In starved cells, approximately 20% of FIP200 puncta colocalized with PIS-GFP almost completely (Fig 6A right top panels, and C), whereas more than 50% of FIP200 puncta only partially associated with PIS-GFP-positive structures (Fig 6A right bottom panels, and C). These results indicate that FIP200 at least partially colocalizes with PIS-GFP even under wortmannin-untreated condition. By contrast, most FIP200 puncta colocalized with PIS-GFP puncta in wortmannin-treated starved cells (Fig 6B and C), which is consistent with that observed by conventional confocal microscopy (Fig 5A and B).

Next, we investigated puncta formation of the ULK complex in live cells. Live imaging analysis of super enhanced cyan fluorescent protein (SECFP)-PIS showed that Venus-ULK1 puncta were formed on SECFP-PIS puncta (Figs 7A and B and Movie EV1 and 2). Before disappearance of the ULK1 signal, a part of the ULK1 structures seemed to dissociate from the PIS puncta (yellow arrows in Fig 7A and B), which suggests a translocation of the ULK complex to distinct autophagosome precursors. Quantitative analysis revealed that more than 50% of Venus-ULK1 puncta emerged on the PIS puncta (Fig 7C). The remaining ULK1 puncta were formed on PIS-positive reticular structures, which may represent similar ER subdomains but the amount of PIS was not large enough to be detected as puncta (Figs 7C and Movie EV3). Considering

that the colocalization ratio between the ULK complex components and PIS puncta was relatively higher in wortmannin-treated cells (Figs 5A and B and 6) and in ATG14 KO cells (Fig 5A), autophagy inhibition at early stages likely causes accumulation of PIS (and other enzymes such as CPT1 and CEPT1) at the autophagosome formation site. Collectively, these results suggest that the ULK complex forms a punctate structure on PIS-enriched ER subdomain at an early stage of autophagy.

PI is required for isolation membrane formation

We finally sought to examine whether PI in the PIS-enriched membrane is required for autophagy. Since RNAi-mediated knockdown of PIS did not induce significant reduction in the cellular PI level (unpublished observations), *Listeria monocytogenes* PI-specific phospholipase C (PIPLC), which degrades unphosphorylated PI, was used to deplete PI (Kim et al, 2011). To validate the effect of PIPLC, cell homogenates were incubated with recombinant PIPLC and subjected to lipid analysis. The level of PI was significantly reduced in the presence of recombinant PIPLC, whereas the levels of other phospholipids were not affected (Fig EV5A), indicating that PIPLC can specifically degrade PI *in vitro*. To target PIPLC to the PIS-enriched membrane *in vivo*, we engineered cells that express PIPLC fused to a catalytic inactive mutant of PIS H105Q (PISHQ) under the control of doxycycline (PISHQ-GFP-PIPLC MEFs). Forced expression of PISHQ-GFP-PIPLC was effective and reduced the level of PI (Fig 8A). In contrast, the levels of other phospholipids were relatively maintained or increased as a compensatory reaction (Fig EV5B). In these cells expressing PISHQ-GFP-PIPLC, although the cellular PI level was reduced to only ~50% of that in DOX-untreated cells, autophagic activity was profoundly suppressed; starvation-induced LC3 turnover and p62 degradation were inhibited (Fig 8B). Furthermore, FIP200-positive but PI3P-binding WIPI2-negative abnormal autophagic structures accumulated (Fig 8C and D). By contrast, the number of WIPI2-positive puncta was significantly reduced by the expression of PISHQ-GFP-PIPLC (Fig 8D-F), suggesting that PI production at the PIS domain is important for autophagosome formation. In these cells, punctate structures labeled with RFP-2xFYVE, a PI3P probe that primarily labels endosomes were also abolished, suggesting a reduction in not only autophagosomal but also the total cellular PI3P level (Fig 8F). On the other hand, cytosolic PIPLC did not affect the formation of WIPI2 puncta (Fig 8G). These data suggest that PI produced at the PIS-enriched subdomain actively contributes to autophagy initiation through a direct effect on autophagic structures and/or indirect effects on other membrane compartments.

DISCUSSION

In this study, we biochemically analyze the membranes carrying upstream ATG proteins and found that FIP200 can be recruited to two different membranes: the ER-related membrane and the isolation membrane carrying ATG9A. We also identified the PIS-enriched ER subdomain as a site for the initiation of autophagosome formation. Furthermore, we showed that PI reduction in the PIS-enriched membrane significantly inhibited autophagosome formation. Based on these results, we hypothesize that the autophagy-initiating ULK complex first translocates to the PIS-enriched ER subdomain in an ATG9A- and PI 3-kinase-independent manner (Fig 8H). Next, ATG9A-containing vesicles, which could be a seed for autophagosome biogenesis, associate with this domain, and the ULK complex translocates to ATG9A vesicles to elongate the membrane.

The ULK complex targets to two distinct membranes: the ER-related membrane and ATG9A-enriched membrane

We have shown that ATG proteins are floated into membrane fractions derived from ATG KO cells (Fig 1). To our knowledge, this is the first systematic biochemical analysis of membrane association status of endogenous ATG proteins. We have also demonstrated the physical interaction of ULK complex component with the ER membrane and ATG9A-positive isolation membrane (Figs 2 and 3). As well as in yeast (Yamamoto et al, 2012), our results suggest that the ATG9A vesicle can be a seed membrane of the autophagosome in mammals. However, our results do not necessarily rule out the possibility that mammalian ATG9A fulfills other functions by its transient interaction with autophagic membranes (Orsi et al, 2012; Lamb et al, 2016), rather than acting only as a seed membrane of the autophagosome. Currently, it is not clear why the ULK complex needs to be recruited to the ER membrane in addition to ATG9A-positive membranes. One possibility is that the ULK complex might induce reorganization of the ER membrane and stimulate the formation of membrane contacts between the ER and ATG9A vesicles. In line with this model, it was recently reported that Atg1 kinase complex can tether Atg9-vesicles *in vitro* experiments (Rao et al, 2016). A similar mechanism might mediate tethering between the ER and ATG9A vesicles.

The recruitment mechanism of the ULK complex seems to be complicated. Consistent with a previous report that Atg17, a yeast counterpart of FIP200, can be recruited to pre-autophagosomal structure in *atg1Δ* and *atg13Δ* cells (Suzuki et al, 2007),

FIP200 has an ability to associate with membranes independently of the other ULK complex components (Fig EV1). It is also possible that FIP200 is recruited to the membrane via its interaction with the ATG12—ATG5—ATG16L1 complex (Fujita et al, 2013; Gammoh et al, 2013; Nishimura et al, 2013), which further interacts with WIPI2 (Dooley et al, 2014). A part of WIPI2 can associate with membranes even in the presence of wortmannin (Polson et al, 2010). By contrast, previous studies showed that other Atg1/ULK complex components have lipid-binding domains. For example, the N terminus of ATG13 interacts with acidic phospholipids (Karanasios et al, 2013). The EAT domain of yeast Atg1 can be co-precipitated with small unilamellar vesicles (Ragusa et al, 2012) and Atg1 also shows high affinity with PI-containing liposomes *in vitro* (Rao et al, 2016). During autophagosome formation, the ULK complex seems to translocate from the ER to ATG9A vesicles, potential autophagosome precursors (Fig 7A and B), although we do not rule out a possibility that additional cytosolic ULK complexes are also directly recruited. This change may be caused by production of PI3P because PI 3-kinase activity is known to stabilize the ULK1 complex on the autophagic membranes (Karanasios et al, 2013). Furthermore, the ULK complex components interact with ATG8 family proteins and are recruited to autophagic membranes dependently on their LC3-interacting region motifs (Alemu et al, 2012). All these factors could determine the unique behavior of the Atg1/ULK complex.

We previously reported that ULK1, ATG13, FIP200, and ATG101 form a stable complex in the cytosol (Hosokawa et al, 2009a; Hosokawa et al, 2009b). By contrast, in the present study, behaviors of ATG13 and FIP200 are somewhat different from that of ULK1. One possibility is that FIP200 and ATG13 could associate with the membrane more tightly than ULK1 and, therefore, ULK1 is released from the membranes during sample preparation and flotation experiments. Another possibility is that the stoichiometry of the complex subunits is different between the cytosolic and membrane complexes.

Contribution of PIS-enriched ER subdomains in the initiation stage of autophagy

We have uncovered that early autophagic structures are formed in close apposition to the PIS-enriched ER subdomains. In wortmannin-treated condition (Fig 4) and ATG14KO cells (unpublished observations), other phospholipid biosynthetic enzymes, such as PSS1, CPT1, CEPT1 and PLD1A, were also co-localized with the ULK complex. Inhibition of autophagosome formation at an early stage might affect local phospholipid metabolism and induce recruitment of phospholipid biosynthetic enzymes to the autophagosome formation site via an unknown feedback loop. While only PIS

clearly shows punctate structures that co-localize with the ULK complex in wortmannin-untreated cells, we speculate that other enzymes are also present at the same membrane at undetectable levels to facilitate autophagosome formation. The involvement of other phospholipid biosynthetic enzymes in autophagy have been investigated. CPT1 positively regulates autophagosome formation under oleic acid-treated conditions (Dupont et al, 2014). The role for PLD1 is rather controversial; it could regulate autophagy either positively or negatively (Dall'Armi et al, 2010; Bae et al, 2014; Jang et al, 2014; Holland et al, 2016). How these enzymes contribute to autophagy initiation, autophagosome formation, or autophagosome maturation remains to be determined in more detail.

The presence of phospholipid biosynthetic enzymes at the site of autophagosome formation suggests that newly synthesized PI and other phospholipids are directly used for autophagosome formation. Consistent with this idea, we showed that PI in the PIS-enriched membrane is required for autophagosome formation (Fig 8B-E). However, as the total cellular PI3P level was also reduced by expression of PISHQ-GFP-PIPLC (Fig 8F), we cannot rule out a possibility that PI depletion affects autophagosome formation through an indirect effect on other membranes. Membrane contacts between the ER membrane and the isolation membrane have been observed by EM analysis in several previous studies (Kovacs et al, 2007; Hayashi-Nishino et al, 2009; Yla-Anttila et al, 2009; Uemura et al, 2014). There is accumulating evidence that phospholipids are synthesized and transported at membrane contact sites between ER and other organelles (Drin, 2014; Prinz, 2014; Raiborg et al, 2015; Levine & Patel, 2016; Phillips & Voeltz, 2016). Therefore, contact sites between the ER and ATG9A-enriched membranes might facilitate transport of newly synthesized PI and other phospholipids between these two compartments. **However, factors involved in non-vesicular lipid transport between the ER and ATG9A-enriched membranes remain unidentified. Future studies are needed to elucidate if lipid transfer proteins contribute to autophagosome formation.**

MATERIALS AND METHODS

Plasmids, antibodies, and reagents

cDNAs encoding the full-length of PIS (NP_080914, Open biosystems, Huntsville, AL), CPT1 (NP_064629, Open biosystems), EPT1 (NP_277040, Kazusa DNA Research Institute, Chiba, Japan), CEPT1 (NP_001007795, Open biosystems), ECT (NP_001171846), CCT β 2 (NP_004836), PSS1 (NP_055569), PSS2 (NP_110410), PSD (NP_055153), PEMT (NP_680477), CDS1 (NP_001254), CDS2 (NP_003809), PLD1A (NP_002653, Kazusa DNA Research Institute), PLD2 (NP_002654, Kazusa DNA Research Institute), DGAT1 (NP_036211), DGAT2 (NP_115953), LIPIN1A (NP_663731), LIPIN1B (NP_056578, Open biosystems), LIPIN2 (NP_055461), LPAAT1/AGPAT1 (NP_116130), LPAAT2/AGPAT2 (NP_006403), LPAAT3/AGPAT3 (NP_064517), AGPAT5 (NP_060831), GPAT1 (NP_065969), GPAT3 (NP_116106), GPAT4 (NP_848934), LPCAT1 (NP_079106), LPCAT2 (NP_060309), LPCAT3/MBOAT5 (NP_005759), LPEAT1/MBOAT1 (NP_001073949), LPEAT2/LPCAT4 (NP_705841), PGS (NP_077733), LPIAT1/MBOAT7 (NP_077274), LCLAT1/LYCAT (NP_872357), LPGAT1 (NP_055688), PTPMT1 (NP_783859, Kazusa DNA Research Institute), SEC61B (NP_006799), and ATG14 (NP_055739) were amplified by PCR and subcloned into pMRX-IP backbone vectors together with the EGFP or FLAG tag. PIS cDNA was cloned into pMRX-IP with SECFP (provided by Atsushi Miyawaki, Riken) to generate pMRX-IP-SECFP-PIS. mRFP-2xFYVE was subcloned into pMRX-IP vector. ATG9A (NP_076990) was subcloned into N-TAP-MXs-puro vector (Yamaguchi et al, 2013). *Listeria monocytogenes* PIPLC cDNA (Kim et al, 2011) was subcloned into pGEX-6P-3 vector (GE Healthcare, Piscataway, NJ). pMRX-IP-PIS(H105Q)-GFP was generated by inverse PCR. For generation of pCW57.1-PISHQ-GFP-PIPLC and pCW57.1-RFP-PIPLC plasmid, PIS(H105Q)-GFP, PIPLC, and RFP-PIPLC were subcloned into pCW57.1 backbone vector. pMRX-IP-Venus-ULK1 plasmid has been previously described (Koyama-Honda et al, 2013). Antibodies used for immunoblotting: rabbit polyclonal anti-FIP200 (17250-1-AP, Protein Tech, Chicago, IL), anti-ATG13 (SAB4200100, Sigma-Aldrich, St. Louis, MO), anti-ATG101 (Hosokawa et al, 2009b), anti-ULK1 (A7481, Sigma-Aldrich), anti-ATG9A (Itakura et al, 2012), anti-ATG14 (Itakura et al, 2008), anti-WIPI2 (SAB4200400, Sigma-Aldrich), anti-ATG5 (A0731, Sigma-Aldrich), anti-LC3 (#1) (Hosokawa et al, 2006), anti-ERGIC53 (E1031, Sigma-Aldrich), anti-SEC61B (07-205, Millipore, Billerica, MA), anti-FLAG (F7425, Sigma-Aldrich), anti-RAB1A (C-19, Santa Cruz, Dallas, TX), anti-GFP (A6455, Invitrogen, Carlsbad,

CA), anti-ATG3 (A3231, Sigma-Aldrich), anti-p62 (PM045, MBL, Nagoya, Japan), anti-VPS34 (#3811, Cell Signaling, Beverly, USA), and anti-BECLIN1 (#3738, Cell Signaling) antibodies, mouse monoclonal anti-HSP90 (clone 68, BD Biosciences, San Jose, CA), anti- β ACTIN (clone AC74, Sigma-Aldrich), anti-LC3 (clone 1703, Cosmo bio, Tokyo, Japan), anti-FLAG (clone M2, Sigma-Aldrich) and anti-DYKDDDK (clone 1E6, Wako, Osaka, Japan) antibodies were used. Antibodies used for immunostaining: rabbit polyclonal anti-FIP200 (see above) and anti-ERGIC53 (see above) antibodies, mouse monoclonal anti-SEC31A (clone 32, BD Biosciences) and anti-WIPI2 (clone 2A2, Millipore) antibodies, AlexaFluor 488-conjugated anti-rabbit IgG, AlexaFluor 568-conjugated anti-mouse IgG and anti-rabbit IgG, and AlexaFluor 660-conjugated anti-mouse IgG and anti-rabbit IgG secondary antibodies (Molecular Probes, Eugene, OR) were used. Doxycycline hydrochloride (Dox) and wortmannin were purchased from Sigma-Aldrich. Bafilomycin A₁ was purchased from Wako.

Cell culture and transfection

ATG14 KO (Nishimura et al, 2013), ATG3 KO (Sou et al, 2008), FIP200 KO (Gan et al, 2006), ATG13 KO (Kaizuka & Mizushima, 2015), ATG101 KO (Suzuki et al, 2015), ULK1/2 DKO (Cheong et al, 2011), and ATG9A KO MEFs (Saitoh et al, 2009) were generated previously. Stable cell lines were generated as follows: HEK293T cells were transiently transfected using Lipofectamine 2000 (Invitrogen) reagent with the indicated retrovirus vector (pCG-VSV-G and pCG-gag-pol for retrovirus infection) or lentivirus vector (pCW57-PISHQ-GFP-PIPLC, pCMV-VSVG, and psPAX2 for lentivirus infection). WT and ATG3 KO MEFs were also transfected using the indicated retrovirus or lentivirus. Cells were cultured in DMEM supplemented with 10% fetal bovine serum (FBS) in a 5% CO₂ incubator. For starvation treatment, cells were washed twice with phosphate-buffered saline (PBS) and incubated in amino acid-free DMEM without FBS (starvation medium).

Optiprep flotation analysis

Cells from four to eight 10-cm dishes were harvested and washed twice with ice-cold PBS. The cell pellets were collected after centrifugation at 600 \times g for 5 min and resuspended in 2 ml ice-cold homogenization buffer (250 mM sucrose, 20 mM Hepes-KOH (pH7.4), 1 mM EDTA, 1 mM phenylmethanesulfonyl fluoride, complete EDTA-free protease inhibitor (Roche, Indianapolis, IN)). Cells were then disrupted by N₂ cavitation (Parr Instrument, Moline, IL) (800 psi, 10 min, 4°C). The homogenized cells were centrifuged twice at 3,000 \times g for 10 min to remove cell debris and

undisrupted cells. The supernatant was diluted with an equal volume of OptiPrep (Sigma, St. Louis, MO). Discontinuous OptiPrep gradients were generated in SW41 tubes (Beckman Instruments, Berkeley, CA) by overlaying the following OptiPrep solutions all in homogenization buffer: 2.4 ml of the diluted supernatant in 30% OptiPrep, 2.4 ml in 25%, 2.4 ml in 20%, 2 ml in 15%, 2 ml in 10%, 0.5 ml in 5%, and 0.5 ml in 0%. The gradients were centrifuged at $150,200 \times g$ in SW41Ti rotors (Beckman Instruments) for 3 h and subsequently 14 fractions (0.85 ml each) were collected from the top. Fractions were diluted with an equal volume of homogenization buffer and membranes were enriched by centrifugation at $100,000 \times g$ for 40 min. The pellets were solubilized with SDS-PAGE sample buffer and heated at 55°C for 10 min.

Immunoisolation of membrane fractions

Anti-FLAG magnetic beads were prepared according to the manufacturer's instructions. In brief, 1 mg NHS-FG magnetic beads (TAS8848N1141, Tamagawa Seiki, Nagano, Japan) was pre-treated with methanol and incubated with 100 μl anti-FLAG M2 or anti-DYKDDDDK antibodies (0.25 $\mu\text{g}/\mu\text{l}$, dissolved in 25 mM MES-NaOH, pH6.0) at 4°C for 30 min. The magnetic beads were treated with 1 M ethanolamine to block unreacted NHS-ester groups at 4°C for 16 h, washed three times in washing buffer (10 mM HEPES-KOH (pH7.9), 50 mM KCl, 1 mM EDTA, 10% glycerol), and stored in 200 μl washing buffer at 4°C until use. Anti-FLAG magnetic beads and 1.5 ml tubes (MS-4215M, Sumitomo Bakelite, Akita, Japan) were blocked with homogenization buffer containing 250 mM NaCl and 1% BSA for 1 h at 4°C . MEFs stably expressing the indicated FLAG-tagged protein were subjected to Optiprep flotation analysis as described above. 400 μl of the indicated fractions were mixed with 20 μl 5 M NaCl and 20 μl anti-FLAG magnetic beads (50% slurry), and rotated for 2 h at 4°C . The magnetic beads were washed four times with homogenization buffer containing 250 mM NaCl and 1% BSA. The magnetic beads were transferred to a new 1.5 ml tube and washed with homogenization buffer containing 250 mM NaCl. The immunoprecipitated membranes were solubilized with 60 μl of $1 \times$ SDS-PAGE sample buffer and heated at 55°C for 10 min.

Immunoblotting

Cells were collected in ice-cold PBS by scraping and precipitated by centrifugation at $1,000 \times g$ for 3 min. Precipitated cells were suspended in 0.1 ml homogenization buffer and homogenized by sonication (3×5 s; Astrason, XL2020 (Misonix, Inc., Farmingdale, NY)). After centrifugation at $1,000 \times g$ for 20 min, the protein concentration of the

supernatant was determined using the BCA method (Pierce Chemical Co., Rockford, IL), mixed with SDS-PAGE sample buffer, and heated at 55°C for 10 min. Samples were subsequently separated by SDS-PAGE and transferred to Immobilon-P polyvinylidene difluoride membranes (Millipore). Immunoblot analysis was performed with the indicated antibodies and visualized with Super-Signal West Pico Chemiluminescent substrate (Pierce Chemical Co.) or Immobilon Western Chemiluminescent HRP substrate (Millipore). Signal intensities were analyzed using the LAS-4000mini image analyzer (GE Healthcare).

Lipid analysis

Recombinant PIPLC was prepared as follows. pGEX6P-3-PIPLC were transformed into E.coli strain BL21. GST-PIPLC expression was induced with 0.5 mM IPTG at 18°C. GST-PIPLC recombinant protein was purified with glutathione-Sepharose (GE Healthcare) and cleaved from GST using PreScission protease (50 mM Tris-HCl (pH 7.4), 400 mM NaCl, 1 mM EDTA, 1 mM dithiothreitol, and 0.1 U/ μ l PreScission protease). Untagged PIPLC protein was dialyzed with PBS for 3 days and stored at -80°C. Phospholipids were extracted using the methanol method (Zhao & Xu, 2010). In brief, methanol was added into cell pellets, sonicated in a bath sonicator for 2 min, and centrifuged at 15,000 \times g for 10 min. The supernatant was applied to Cosmospin Filter G (Nacalai Tesque, Kyoto, Japan) and centrifuged at 5,000 \times g for 5 min. 10 μ l of sample was injected into the LC-ESI-MS/MS system. LC-ESI-MS/MS analysis was performed using a Shimadzu Nexera ultra high performance liquid chromatography system (Shimadzu, Kyoto, Japan) coupled with a QTRAP 4500 hybrid triple quadrupole linear ion trap mass spectrometer (AB SCIEX, Toronto, Canada). Chromatographic separation was performed on an Acquity UPLC HSS T3 column (100 mm \times 2.1 mm, 1.8 μ m; Waters) maintained at 40°C using mobile phase A (water/methanol (50/50, v/v) containing 10 mM ammonium acetate and 0.2% acetic acid) and mobile phase B (isopropanol/acetone (50/50, v/v)) in a gradient program (0–3 min: 30% B \rightarrow 50% B; 3–24 min: 50% B \rightarrow 90% B; 24–28 min: 30% B) with a flow rate of 0.3 ml/min. Neutral loss scans of 74 and 87 Da in the negative ion mode were used to detect phosphatidylcholine and phosphatidylserine, respectively. Precursor ion scan of m/z 196, 241, 153, and 384 in the negative ion mode was used to detect phosphatidylethanolamine, phosphatidylinositol, phosphatidic acid, and cytidine diphosphate-diacylglycerol, respectively. The total cycle time was 1.7 s, which allowed the collection of sufficient data points over the chromatographic peak. The instrument parameters were as follows: curtain gas, 10 psi; collision gas, 7 arb. unit; ionspray

voltage, -4500 V; temperature, 700°C; ion source gas 1, 30 psi; ion source gas 2, 70 psi; declustering potential, -96 V; entrance potential, -10 V; collision energy, -36 V; collision cell exit potential, -15.4 V.

Fluorescence microscopy

Cells grown on coverslips were fixed with 4% paraformaldehyde, permeabilized using 50 µg/ml digitonin, and then stained with specific antibodies. For mitochondrial staining, cells were pretreated with 50 nM Mitotracker Red CMXRos (Molecular Probes) for 15 min before fixation. For ERGIC53 staining, cells were fixed with methanol. These cells were observed using a confocal laser microscope FV1000D IX81 (Olympus, Tokyo, Japan) with FV12-HSD system using a 60x PlanApoN oil immersion lens (1.42 NA; Olympus). Images were acquired at room temperature using FV10-ASW software (Olympus). For the final output, images were processed using Adobe Photoshop 7.0.1 software. The number of dots was determined using MetaMorph software (Molecular Devices, Sunnyvale, CA) as follows: dots were extracted using the top hat operation, and a binary image was created. Small dots were removed using an open operation. The number of dots was counted using the integrated morphometry analysis program. False dots were removed by comparison with the original image.

Super-resolution structured illumination microscopy (SR-SIM)

Super-resolution imaging was performed on a Zeiss Elyra PS.1 microscope equipped with a Plan-Apochromat 63× /1.4 oil DIC M27 objective and a sCMOS camera (1280 x 1280 pixels of 6.5 x 6.5 µm). Fifteen images per plane (5 phases and 3 angles) were acquired with the 561 nm (34 µm grating period) and the 488 nm (28 µm gating period) lasers. For channel alignment, 0.2-µm multicolored beads immobilized on a sample coverslip were imaged using the same image acquisition settings and used to correct for chromatic shifts between different color channels. Raw data was processed using Zeiss Zen software.

Live-cell imaging

For autophagy induction, cells were washed twice with PBS and incubated in starvation medium. Images were acquired with a 60× PlanAPO oil-immersion objective lens (1.42 NA; Olympus), using a Deltavision microscope system (GE Healthcare) coupled with an Olympus IX81-ZDC and a cooled CCD camera CoolSNAP HQ2 (Photometrics, Tucson, AZ). WT MEFs stably expressing SECFP-PIS and Venus-ULK1 were grown on a glass bottom dish (11-004-006) (IWAKI, Tokyo, Japan). During live-cell imaging,

the culture dish was mounted in a chamber INUB-ONI-F2 (TOKAI HIT, Shizuoka, Japan) to maintain the culture conditions (37°C and 5% CO₂). SECFP-PIS and Venus-ULK1 were illuminated with a mercury arc lamp attenuated to 5% and 50% by neutral density filters, respectively. Exposure times were 0.2 s for SECFP-PIS and 0.5 s for Venus-ULK1. Time-lapse images were acquired at 10-s intervals. Deconvoluted images were obtained using softWoRx software. To find newly formed ULK1, sequential images were subjected to single-particle tracking analysis using MetaMorph software. For the final output, images were processed using Image J and Adobe Photoshop 7.0.1 software.

Data analysis

Differences were statistically analyzed by two-tailed Mann-Whitney U-test. Statistical analysis was carried out using GraphPad Prism 6 (GraphPad Software, La Jolla, CA). All data are presented as the mean ± SEM. Reproducibility of all results reported here was confirmed.

ACKNOWLEDGEMENTS

We are grateful to Lo Yu Chia for technical assistance. We thank Tatsuya Saitoh and Shizuo Akira for providing ATG14 KO and ATG9A KO MEFs, Masaaki Komatsu for ATG3 KO MEFs, Jun-Lin Guan for FIP200 KO MEFs, Craig B. Thompson for ULK1/2 DKO MEFs, Shoji Yamaoka for the retroviral vectors, Atsushi Miyawaki for the plasmid coding SECFP, Teruhito Yasui for the pCG-VSV-G and pCG-gag-pol plasmids, Noritaka Yamaguchi for the N-TAP-MXs-puro plasmid, Hideo Shindou and Takao Shimizu for the LPCAT1 cDNA, Kazusa DNA Research Institute for the PLD1A, PLD2, and EPT1 cDNAs, Harald Stenmark for mRFP-2xFYVE, Tamas Balla for the mRFP-PI-PLC plasmid, David Root for the pCW57.1 plasmid, Didier Trono for the psPAX2 plasmid, and Robert A. Weinberg for the pCMV-VSV-G plasmid. We also thank Ikuko Koyama-Honda for technical support with live imaging analysis, Takeshi Harayama for helpful discussion about phospholipid biosynthesis pathways and Christopher J. Stefan for helpful discussion. This work was supported by Japan Society for the Promotion of Science KAKENHI Grant-in-Aid for Young Scientists (A) 26711011 (to T.N.), Grant-in-Aid for Scientific Research (S) 23227004 (to H.A.) and Grant-in-Aid for Scientific Research on Innovative Areas 25111005 (to N.M.) from MEXT, AMED-CREST (to H.A.) from AMED, the Naito Foundation (to T.N.), a grant from the Japan Foundation for Applied Enzymology (to T.N.), and MRC funding to the

MRC LMCB University Unit at UCL, award code MC_U12266B.

AUTHOR CONTRIBUTIONS

T.N. and N.M. designed the experiments; T.N., N.T. and H.Y. performed the experiments; N.K., Y.S. and H.A. contributed to lipid analysis; T.N., N.T., N.K., H.Y. and N.M. analyzed the data; and T.N. and N.M. wrote the manuscript. All authors discussed the results and commented on the manuscript.

CONFLICT OF INTEREST

The authors declare no competing financial interests.

ABBREVIATION LIST

ATG, autophagy-related; ULK, unc-51-like kinase (*C. elegans*); FIP200, FAK family kinase-interacting protein 200 kDa; WIPI, WD repeat domain, phosphoinositide interacting; ER, endoplasmic reticulum; ERGIC, ER-Golgi intermediate compartment; MEFs, mouse embryonic fibroblasts; LC3, microtubule-associated protein light chain 3; GFP, green fluorescent protein; SECFP, super enhanced cyan fluorescent protein; mRFP, monomeric red fluorescent protein; WM, wortmannin; PIS, phosphatidylinositol synthase; CPT1, cholinephosphotransferase 1; CEPT1, choline/ethanolaminephosphotransferase 1; PSS1, phosphatidylserine synthase 1; PLD1A, phospholipase D1A; PIPLC, PI-specific phospholipase C.

Figure legends

Figure 1. Flotation of ATG proteins derived from ATG14 KO and ATG3 KO cell homogenates.

(A) Optiprep membrane flotation analysis of WT MEFs cultured in regular DMEM (Growing). After fractionation, each fraction was centrifuged at $100,000 \times g$ for 40 min to enrich the membranes.

(B) Autophagosome formation. ATG14 and ATG3 are required for the nucleation and elongation or closure steps during autophagosome formation, respectively.

(C, D) ATG14 KO (C) and ATG3 KO MEFs (D) were cultured in regular DMEM and subjected to Optiprep flotation analysis as described above. Asterisks indicate the flotation of ATG proteins of ATG14 KO and ATG3 KO homogenates. Arrow indicates the position of ATG14 (A, D).

(E, F) ATG3 KO MEFs stably expressing FLAG-ATG9A were cultured in regular DMEM (E) or starvation medium in the presence of 200 nM wortmannin (Starv. + WM) (F) for 2 h. Note that wortmannin treatment significantly reduced the amounts of the ULK complex components, WIPI2, and ATG5 in the top fraction (compare † in E with †† in F).

Figure 2. FIP200 is co-purified with the ER membranes from ATG14 KO MEF homogenates.

(A) Experimental scheme of autophagic membrane purification. Cells stably expressing FLAG-ATG9A were cultured in regular DMEM and subjected to Optiprep flotation analysis. FLAG-ATG9A-enriched membranes were precipitated from the middle density fractions (Fr. 4-7 mixture) or the top fraction (Fr. 1) under detergent-free conditions using anti-FLAG antibody-coated magnetic beads.

(B, C) Purification of ATG9A-positive membranes. WT (B) and ATG14 KO MEFs (C) expressing FLAG-ATG9A were cultured in regular DMEM and subjected to Optiprep flotation analysis as described in the legend to Fig 1. FLAG-ATG9A-enriched membranes were purified from middle-density fractions derived from WT (B) (Fig EV2A) and ATG14 KO MEF homogenates (C) (Fig EV2B). The resulting precipitates were examined by immunoblot analysis with the indicated antibodies.

(D) The ER membranes were purified from middle-density fractions derived from ATG14 KO MEF homogenates by immunoprecipitation with FLAG-GFP-SEC61B. **An asterisk indicates non-specific signals.** The intensities of the bands in the input and IP fractions were measured using Image J software. The ratio of IP to input was calculated.

Each value was normalized to the ratio of IP to input of FLAG-tagged protein (co-IP efficiency).

Figure 3. FIP200 and the ER membrane are co-purified with ATG9A-positive membranes from ATG3 KO MEF homogenates.

(A-C) Purification of ATG9A-positive membranes. ATG3 KO MEFs expressing indicated constructs were cultured in regular DMEM and subjected to Optiprep flotation analysis as shown in Fig 1E. FLAG-ATG9A-enriched membranes were purified from the top fraction (Fraction 1) (A) and middle-density fractions (Fractions 4-7) (B, C).

The immunoprecipitation efficiency was calculated as in Figure 2.

(D) Summary of autophagic membrane purification. FIP200 was co-precipitated with the ER membranes purified from middle density fractions of ATG14 KO homogenates (ATG14 KO, Fr. 4-7) (Fig 2D). The FLAG-ATG9A immunoprecipitates from the middle-density fractions of ATG3 KO homogenates contained the ER marker SEC61B and GFP-ATG14 as well as small amounts of FIP200 and WIPI2, which might reflect the ER-isolation membrane contact (ATG3 KO, Fr. 4-7) (Fig 3B, C). FIP200 and the isolation membrane protein WIPI2 were co-precipitated with ATG9A-enriched membrane from the top fraction of ATG3 KO homogenates (ATG3 KO, Fr. 1) (Fig 3A).

Figure 4. Several phospholipid biosynthetic enzymes colocalize with FIP200 in wortmannin-treated cells under starvation conditions.

(A) The phospholipid synthesis pathways in mammalian cells. *De novo* synthesis (top) and remodeling (bottom) pathways are shown. Enzymes that colocalize with endogenous FIP200 in WT MEFs cultures in starvation medium in the presence of 200 nM wortmannin for 1 h are shown in red, and those that do not colocalize are shown in blue.

(B) WT MEFs stably expressing the indicated GFP- or FLAG-tagged enzymes were cultured in starvation medium in the presence or absence of 200 nM wortmannin for 1 h. The cells were fixed and stained with anti-FIP200 antibody. Subcellular distributions of the indicated enzymes and FIP200 were examined by immunofluorescence microscopy. The cells were classified into three categories based on the colocalization of the indicated enzyme and FIP200: Clear colocalization (red), partial colocalization (green), and no colocalization (blue). More than 30 cells were analyzed for each protein.

Figure 5. FIP200 is recruited to PIS-enriched ER subdomains at the initiation stage of autophagy.

(A) WT or ATG14 KO MEFs stably expressing PIS-GFP were cultured in regular DMEM or starvation medium in the presence of wortmannin (WM) for 1 h.

(B) Quantification of the number of FIP200⁺PIS⁻ and FIP200⁺PIS⁺ puncta in growing cells and wortmannin-treated starved cells. The number of puncta was quantified from more than 60 randomly selected cells from three independent samples as described in the Methods. Data represent mean \pm SEM. * $P < 0.0001$ vs. growing condition.

(C) HeLa cells stably expressing PIS-GFP were cultured in starvation medium in the presence of wortmannin for 1 h. Cells were analyzed by immunofluorescence microscopy using anti-FIP200 and anti-SEC31A antibodies.

(D) WT MEFs stably expressing PIS-GFP were cultured in starvation medium in the presence of wortmannin for 1 h. For mitochondrial staining, cells were treated with 50 nM Mitotracker Red CMXRos for 15 min before fixation. Scale bars, 10 μ m (A, C, and D).

(E) PIS-GFP-FLAG was precipitated from the middle-density fractions of ATG14 KO MEF homogenates in the absence or presence of 1% Triton X-100. The resulting precipitates were examined by immunoblot analysis with the indicated antibodies.

Figure 6. Super-resolution structured illumination microscopy of association of FIP200 with the PIS-enriched ER subdomains.

(A, B) WT MEFs stably expressing PIS-GFP were cultured in starvation medium in the absence (A) or presence (B) of wortmannin (WM) for 1 h. The cells were fixed and stained with anti-FIP200 antibody.

(C) Quantification of experiments in A and B. FIP200 puncta were classified into three categories: “colocalized” with PIS-GFP, “associated” with (next to) PIS-GFP, and “non-associated” with (away from) PIS-GFP. Experimental conditions are indicated in panels: starvation (St) (A) or starvation with wortmannin (St+WM) (B). More than 100 puncta were analyzed. Scale bars, 5 μ m (A, B), 0.2 μ m (insets, C).

Figure 7. Puncta formation of the ULK complex on PIS-positive structures in live cells.

(A, B) Two representative live-cell time-lapse images of WT MEFs stably expressing Venus-ULK1 and SECFP-PIS. Cells were cultured in starvation medium and observed using a DeltaVision microscopy system. Frames were captured every 10 s. White arrowheads indicate colocalization of Venus-ULK1 with SECFP-PIS. Some Venus-ULK1 puncta were detached from SECFP-PIS puncta at last 2–3 frames before disappearance (indicated by yellow arrowheads) (see Movies EV1 and 2).

(C) Quantification of colocalization of newly formed Venus-ULK1 puncta and PIS-positive punctate or reticular structures. To identify newly formed ULK1 puncta, sequential images were subjected to single-particle tracking analysis. More than 90 areas were analyzed.

Figure 8. PI in the PIS-enriched membranes is required for isolation membrane formation.

(A) PISHQ-GFP-PIPLC MEFs were pre-cultured in the absence or presence of 2 $\mu\text{g/ml}$ doxycycline (DOX) for 4 h to induce PISHQ-GFP-PIPLC expression. The level of PI was measured by liquid chromatography-electrospray ionization-tandem mass spectrometry. Values indicate individual molecular species of PI.

(B) Autophagic flux assay. PISHQ-GFP-PIPLC MEFs were pre-treated with DOX for 8 h and then cultured in regular DMEM or starvation medium in the presence or absence of 100 nM bafilomycin A₁ (BafA₁) for 2 h.

(C, D) PISHQ-GFP-PIPLC MEFs were pre-cultured in the absence or presence of DOX for 4 h and then cultured in starvation medium for 1 h.

(E) Quantification of the number of WIPI2 puncta. In DOX-treated condition, the number of WIPI2 puncta was quantified from the cells expressing PISHQ-GFP-PIPLC. Data present mean \pm SEM. * $P < 0.0001$ vs. DOX-untreated cells.

(F) PISHQ-GFP-PIPLC MEFs stably expressing mRFP-2xFYVE were pre-treated with DOX for 3 h and then cultured in starvation medium with DOX for 1 h.

(G) RFP-PIPLC MEFs were pre-cultured in the absence or presence of DOX for 24 h. Scale bars, 10 μm (C, D, F, and G).

(H) Model of the initial stages of autophagosome formation. The ULK complex translocates to the PIS-enriched ER subdomains and induces recruitment of downstream factors such as ATG14. At least a part of ATG9A is incorporated into the isolation membrane. The PIS-enriched ER membrane supplies PI (and/or PI3P) to ATG9A vesicles or isolation membrane precursors, leading to isolation membrane formation.

Expanded View Figure Legends

Figure EV1. FIP200 is recruited to membrane structures independently of the other ULK complex components and ATG9A.

(A) WT MEFs stably expressing FLAG-ATG9A were cultured in starvation medium for 2 h and subjected to Optiprep membrane flotation analysis as in Fig 1A. Asterisk indicates the fractions of floated Atg proteins.

(B) Validation of ATG KO cell lines. WT and various ATG KO MEFs were analyzed by immunoblotting using the indicated antibodies.

(C-F) FIP200 KO (C), ULK1/2 DKO (D), ATG13 KO (E), and ATG101 KO MEFs (F) were cultured in regular DMEM and subjected to Optiprep membrane flotation analysis. Asterisks indicate the flotation of FIP200 into middle-density fractions.

(G) The indicated ATG KO MEFs were cultured in starvation medium for 1 h and analyzed by immunofluorescence microscopy using anti-FIP200 antibody.

(H) WT MEFs stably expressing GFP-ATG9A were cultured in starvation medium in the presence or absence of 200 nM wortmannin for 1 h. Cells were fixed and analyzed by immunofluorescence microscopy using anti-FIP200 and WIPI2 antibodies. Scale bars, 10 μm (G, H).

Figure EV2. Separation of autophagy-related membranes in ATG9A KO and ATG14 KO cells.

(A-C) The indicated MEF cells were cultured in regular DMEM and subjected to Optiprep flotation analysis as shown in Fig 1E. Asterisks indicate the flotation of FIP200 into middle-density fractions (B, C).

Figure EV3. The effect of starvation on PIS-GFP expression.

WT MEFs stably expressing PIS-GFP were cultured in growing or starvation conditions in the presence of the indicated inhibitor for 4 h. Then, 200 nM wortmannin (WM), 100 nM bafilomycin A₁ (BafA₁), 10 μM MG132, and 5 $\mu\text{g/ml}$ brefeldin A (BFA) were used. Note that p62 but not PIS-GFP was degraded in an autophagy dependent manner under starvation conditions.

Figure EV4. No colocalization of PIS puncta with ERGIC53 in wortmannin-treated cells under starvation conditions.

WT MEFs stably expressing PIS-GFP were cultured in starvation medium in the presence of 200 nM wortmannin for 1 h. Cells were analyzed by immunofluorescence

microscopy using anti-ERGIC53 antibody. Scale bar, 10 μ m.

Figure EV5. Lipid analysis of recombinant PIPLC-treated cell homogenates and PISHQ-PIPLC-expressing cells.

(A) WT MEF homogenates were treated with 6.25 μ g/ml recombinant PIPLC (rPIPLC) for 30 min at 37°C. Phospholipids were extracted by the methanol method and subjected to LC-ESI-MS/MS analysis. The MS spectra of the indicated phospholipids are shown.

(B) PISHQ-GFP-PIPLC MEFs were pre-cultured in the absence or presence of 2 μ g/ml doxycycline (DOX) for 4 h to induce PISHQ-GFP-PIPLC expression. Phospholipids were extracted and analyzed as in (A). The prefix “e” indicates a chain with an ether linkage. Note that CDP-DAG were increased as a compensatory reaction.

PI, phosphatidylinositol; PC, phosphatidylcholine; SM, sphingomyelin; PE, phosphatidylethanolamine; PS, phosphatidylserine; PA, phosphatidic acid; CDP-DAG, cytidine diphosphate-diacylglycerol.

REFERENCES

- Alemu EA, Lamark T, Torgersen KM, Birgisdottir AB, Larsen KB, Jain A, Olsvik H, Overvatn A, Kirkin V, Johansen T (2012) ATG8 family proteins act as scaffolds for assembly of the ULK complex: sequence requirements for LC3-interacting region (LIR) motifs. *J Biol Chem* 287: 39275-39290
- Axe EL, Walker SA, Manifava M, Chandra P, Roderick HL, Habermann A, Griffiths G, Ktistakis NT (2008) Autophagosome formation from membrane compartments enriched in phosphatidylinositol 3-phosphate and dynamically connected to the endoplasmic reticulum. *J Cell Biol* 182: 685-701
- Bae EJ, Lee HJ, Jang YH, Michael S, Masliah E, Min DS, Lee SJ (2014) Phospholipase D1 regulates autophagic flux and clearance of alpha-synuclein aggregates. *Cell Death Differ* 21: 1132-1141
- Chan EY, Longatti A, McKnight NC, Tooze SA (2009) Kinase-inactivated ULK proteins inhibit autophagy via their conserved C-terminal domains using an Atg13-independent mechanism. *Mol Cell Biol* 29: 157-171
- Cheong H, Lindsten T, Wu J, Lu C, Thompson CB (2011) Ammonia-induced autophagy is independent of ULK1/ULK2 kinases. *Proc Natl Acad Sci U S A* 108: 11121-11126
- Dall'Armi C, Hurtado-Lorenzo A, Tian H, Morel E, Nezu A, Chan RB, Yu WH, Robinson KS, Yeku O, Small SA, Duff K, Frohman MA, Wenk MR, Yamamoto A, Di Paolo G (2010) The phospholipase D1 pathway modulates macroautophagy. *Nat Commun* 1: 142
- Dooley HC, Razi M, Polson HE, Girardin SE, Wilson MI, Tooze SA (2014) WIPI2 links LC3 conjugation with PI3P, autophagosome formation, and pathogen clearance by recruiting Atg12-5-16L1. *Mol Cell* 55: 238-252
- Drin G (2014) Topological regulation of lipid balance in cells. *Annu Rev Biochem* 83: 51-77
- Dupont N, Chauhan S, Arko-Mensah J, Castillo EF, Masedunskas A, Weigert R,

Robenek H, Proikas-Cezanne T, Deretic V (2014) Neutral lipid stores and lipase PNPLA5 contribute to autophagosome biogenesis. *Curr Biol* 24: 609-620

English AR, Voeltz GK (2013) Rab10 GTPase regulates ER dynamics and morphology. *Nat Cell Biol* 15: 169-178

Fujita N, Morita E, Itoh T, Tanaka A, Nakaoka M, Osada Y, Umemoto T, Saitoh T, Nakatogawa H, Kobayashi S, Haraguchi T, Guan JL, Iwai K, Tokunaga F, Saito K, Ishibashi K, Akira S, Fukuda M, Noda T, Yoshimori T (2013) Recruitment of the autophagic machinery to endosomes during infection is mediated by ubiquitin. *J Cell Biol* 203: 115-128

Gammoh N, Florey O, Overholtzer M, Jiang X (2013) Interaction between FIP200 and ATG16L1 distinguishes ULK1 complex-dependent and -independent autophagy. *Nat Struct Mol Biol* 20: 144-149

Gan B, Peng X, Nagy T, Alcaraz A, Gu H, Guan JL (2006) Role of FIP200 in cardiac and liver development and its regulation of TNFalpha and TSC-mTOR signaling pathways. *J Cell Biol* 175: 121-133

Ge L, Melville D, Zhang M, Schekman R (2013) The ER-Golgi intermediate compartment is a key membrane source for the LC3 lipidation step of autophagosome biogenesis. *Elife* 2: e00947

Graef M, Friedman JR, Graham C, Babu M, Nunnari J (2013) ER exit sites are physical and functional core autophagosome biogenesis components. *Mol Biol Cell* 24: 2918-2931

Hamasaki M, Furuta N, Matsuda A, Nezu A, Yamamoto A, Fujita N, Oomori H, Noda T, Haraguchi T, Hiraoka Y, Amano A, Yoshimori T (2013) Autophagosomes form at ER-mitochondria contact sites. *Nature* 495: 389-393

Hayashi-Nishino M, Fujita N, Noda T, Yamaguchi A, Yoshimori T, Yamamoto A (2009) A subdomain of the endoplasmic reticulum forms a cradle for autophagosome formation. *Nat Cell Biol* 11: 1433-1437

Holland P, Knaevelsrud H, Soreng K, Mathai BJ, Lystad AH, Pankiv S, Bjorndal GT, Schultz SW, Lobert VH, Chan RB, Zhou B, Liestol K, Carlsson SR, Melia TJ, Di Paolo G, Simonsen A (2016) HS1BP3 negatively regulates autophagy by modulation of phosphatidic acid levels. *Nat Commun* 7: 13889

Hosokawa N, Hara T, Kaizuka T, Kishi C, Takamura A, Miura Y, Iemura S, Natsume T, Takehana K, Yamada N, Guan JL, Oshiro N, Mizushima N (2009a) Nutrient-dependent mTORC1 association with the ULK1-Atg13-FIP200 complex required for autophagy. *Mol Biol Cell* 20: 1981-1991

Hosokawa N, Hara Y, Mizushima N (2006) Generation of cell lines with tetracycline-regulated autophagy and a role for autophagy in controlling cell size. *FEBS Lett* 580: 2623-2629

Hosokawa N, Sasaki T, Iemura S, Natsume T, Hara T, Mizushima N (2009b) Atg101, a novel mammalian autophagy protein interacting with Atg13. *Autophagy* 5: 973-979

Itakura E, Kishi-Itakura C, Koyama-Honda I, Mizushima N (2012) Structures containing Atg9A and the ULK1 complex independently target depolarized mitochondria at initial stages of Parkin-mediated mitophagy. *J Cell Sci* 125: 1488-1499

Itakura E, Kishi C, Inoue K, Mizushima N (2008) Beclin 1 forms two distinct phosphatidylinositol 3-kinase complexes with mammalian Atg14 and UVRAG. *Mol Biol Cell* 19: 5360-5372

Itakura E, Mizushima N (2010) Characterization of autophagosome formation site by a hierarchical analysis of mammalian Atg proteins. *Autophagy* 6: 764-776

Jang YH, Choi KY, Min DS (2014) Phospholipase D-mediated autophagic regulation is a potential target for cancer therapy. *Cell Death Differ* 21: 533-546

Kageyama S, Omori H, Saitoh T, Sone T, Guan JL, Akira S, Imamoto F, Noda T, Yoshimori T (2011) The LC3 recruitment mechanism is separate from Atg9L1-dependent membrane formation in the autophagic response against Salmonella. *Mol Biol Cell* 22: 2290-2300

- Kaizuka T, Mizushima N (2015) Atg13 is essential for autophagy and cardiac development in mice. *Mol Cell Biol*
- Kakuta S, Yamamoto H, Negishi L, Kondo-Kakuta C, Hayashi N, Ohsumi Y (2012) Atg9 vesicles recruit vesicle-tethering proteins Trs85 and Ypt1 to the autophagosome formation site. *J Biol Chem* 287: 44261-44269
- Karanasios E, Stapleton E, Manifava M, Kaizuka T, Mizushima N, Walker SA, Ktistakis NT (2013) Dynamic association of the ULK1 complex with omegasomes during autophagy induction. *J Cell Sci* 126: 5224-5238
- Kihara A, Noda T, Ishihara N, Ohsumi Y (2001) Two distinct Vps34 phosphatidylinositol 3-kinase complexes function in autophagy and carboxypeptidase Y sorting in *Saccharomyces cerevisiae*. *J Cell Biol* 152: 519-530
- Kim YJ, Guzman-Hernandez ML, Balla T (2011) A highly dynamic ER-derived phosphatidylinositol-synthesizing organelle supplies phosphoinositides to cellular membranes. *Dev Cell* 21: 813-824
- Kishi-Itakura C, Koyama-Honda I, Itakura E, Mizushima N (2014) Ultrastructural analysis of autophagosome organization using mammalian autophagy-deficient cells. *J Cell Sci* 127: 4089-4102
- Kovacs AL, Palfia Z, Rez G, Vellai T, Kovacs J (2007) Sequestration revisited: integrating traditional electron microscopy, de novo assembly and new results. *Autophagy* 3: 655-662
- Koyama-Honda I, Itakura E, Fujiwara TK, Mizushima N (2013) Temporal analysis of recruitment of mammalian ATG proteins to the autophagosome formation site. *Autophagy* 9: 1491-1499
- Lamb CA, Nuhlen S, Judith D, Frith D, Snijders AP, Behrends C, Tooze SA (2016) TBC1D14 regulates autophagy via the TRAPP complex and ATG9 traffic. *EMBO J* 35: 281-301
- Levine TP, Patel S (2016) Signalling at membrane contact sites: two membranes come

together to handle second messengers. *Curr Opin Cell Biol* 39: 77-83

Longatti A, Lamb CA, Razi M, Yoshimura S, Barr FA, Tooze SA (2012) TBC1D14 regulates autophagosome formation via Rab11- and ULK1-positive recycling endosomes. *J Cell Biol* 197: 659-675

Mizushima N, Yoshimori T, Ohsumi Y (2011) The role of Atg proteins in autophagosome formation. *Annu Rev Cell Dev Biol* 27: 107-132

Nishimura T, Kaizuka T, Cadwell K, Sahani MH, Saitoh T, Akira S, Virgin HW, Mizushima N (2013) FIP200 regulates targeting of Atg16L1 to the isolation membrane. *EMBO Rep* 14: 284-291

Orsi A, Razi M, Dooley HC, Robinson D, Weston AE, Collinson LM, Tooze SA (2012) Dynamic and transient interactions of Atg9 with autophagosomes, but not membrane integration, are required for autophagy. *Mol Biol Cell* 23: 1860-1873

Papinski D, Schuschnig M, Reiter W, Wilhelm L, Barnes CA, Maiolica A, Hansmann I, Pfaffenwimmer T, Kijanska M, Stoffel I, Lee SS, Brezovich A, Lou JH, Turk BE, Aebersold R, Ammerer G, Peter M, Kraft C (2014) Early steps in autophagy depend on direct phosphorylation of Atg9 by the Atg1 kinase. *Mol Cell* 53: 471-483

Park JM, Jung CH, Seo M, Otto NM, Grunwald D, Kim KH, Moriarity B, Kim YM, Starker C, Nho RS, Voytas D, Kim DH (2016) The ULK1 complex mediates MTORC1 signaling to the autophagy initiation machinery via binding and phosphorylating ATG14. *Autophagy* 12: 547-564

Phillips MJ, Voeltz GK (2016) Structure and function of ER membrane contact sites with other organelles. *Nat Rev Mol Cell Biol* 17: 69-82

Pol A, Gross SP, Parton RG (2014) Review: biogenesis of the multifunctional lipid droplet: lipids, proteins, and sites. *J Cell Biol* 204: 635-646

Polson HE, de Lartigue J, Rigden DJ, Reedijk M, Urbe S, Clague MJ, Tooze SA (2010) Mammalian Atg18 (WIPI2) localizes to omegasome-anchored phagophores and positively regulates LC3 lipidation. *Autophagy* 6: 506-522

- Prinz WA (2014) Bridging the gap: membrane contact sites in signaling, metabolism, and organelle dynamics. *J Cell Biol* 205: 759-769
- Ragusa MJ, Stanley RE, Hurley JH (2012) Architecture of the Atg17 complex as a scaffold for autophagosome biogenesis. *Cell* 151: 1501-1512
- Raiborg C, Wenzel EM, Stenmark H (2015) ER-endosome contact sites: molecular compositions and functions. *EMBO J* 34: 1848-1858
- Rao Y, Perna MG, Hofmann B, Beier V, Wollert T (2016) The Atg1-kinase complex tethers Atg9-vesicles to initiate autophagy. *Nat Commun* 7: 10338
- Russell RC, Tian Y, Yuan H, Park HW, Chang YY, Kim J, Kim H, Neufeld TP, Dillin A, Guan KL (2013) ULK1 induces autophagy by phosphorylating Beclin-1 and activating VPS34 lipid kinase. *Nat Cell Biol* 15: 741-750
- Saitoh T, Fujita N, Hayashi T, Takahara K, Satoh T, Lee H, Matsunaga K, Kageyama S, Omori H, Noda T, Yamamoto N, Kawai T, Ishii K, Takeuchi O, Yoshimori T, Akira S (2009) Atg9a controls dsDNA-driven dynamic translocation of STING and the innate immune response. *Proc Natl Acad Sci U S A* 106: 20842-20846
- Shindou H, Shimizu T (2009) Acyl-CoA:lysophospholipid acyltransferases. *J Biol Chem* 284: 1-5
- Sou YS, Waguri S, Iwata J, Ueno T, Fujimura T, Hara T, Sawada N, Yamada A, Mizushima N, Uchiyama Y, Kominami E, Tanaka K, Komatsu M (2008) The Atg8 conjugation system is indispensable for proper development of autophagic isolation membranes in mice. *Mol Biol Cell* 19: 4762-4775
- Suzuki H, Kaizuka T, Mizushima N, Noda NN (2015) Structure of the Atg101-Atg13 complex reveals essential roles of Atg101 in autophagy initiation. *Nat Struct Mol Biol* 22: 572-580
- Suzuki K, Akioka M, Kondo-Kakuta C, Yamamoto H, Ohsumi Y (2013) Fine mapping of autophagy-related proteins during autophagosome formation in *Saccharomyces*

cerevisiae. *J Cell Sci* 126: 2534-2544

Suzuki K, Kubota Y, Sekito T, Ohsumi Y (2007) Hierarchy of Atg proteins in pre-autophagosomal structure organization. *Genes Cells* 12: 209-218

Uemura T, Yamamoto M, Kametaka A, Sou YS, Yabashi A, Yamada A, Annoh H, Kametaka S, Komatsu M, Waguri S (2014) A cluster of thin tubular structures mediates transformation of the endoplasmic reticulum to autophagic isolation membrane. *Mol Cell Biol* 34: 1695-1706

Xie Z, Klionsky DJ (2007) Autophagosome formation: core machinery and adaptations. *Nat Cell Biol* 9: 1102-1109

Yamaguchi N, Oyama M, Kozuka-Hata H, Inoue J (2013) Involvement of A20 in the molecular switch that activates the non-canonical NF- κ B pathway. *Sci Rep* 3: 2568

Yamamoto H, Kakuta S, Watanabe TM, Kitamura A, Sekito T, Kondo-Kakuta C, Ichikawa R, Kinjo M, Ohsumi Y (2012) Atg9 vesicles are an important membrane source during early steps of autophagosome formation. *J Cell Biol* 198: 219-233

Yla-Anttila P, Vihinen H, Jokita E, Eskelinen EL (2009) 3D tomography reveals connections between the phagophore and endoplasmic reticulum. *Autophagy* 5: 1180-1185

Zhao Z, Xu Y (2010) An extremely simple method for extraction of lysophospholipids and phospholipids from blood samples. *J Lipid Res* 51: 652-659

Zhou C, Ma K, Gao R, Mu C, Chen L, Liu Q, Luo Q, Feng D, Zhu Y, Chen Q (2017) Regulation of mATG9 trafficking by Src- and ULK1-mediated phosphorylation in basal and starvation-induced autophagy. *Cell Res* 27: 184-201

Figure 1

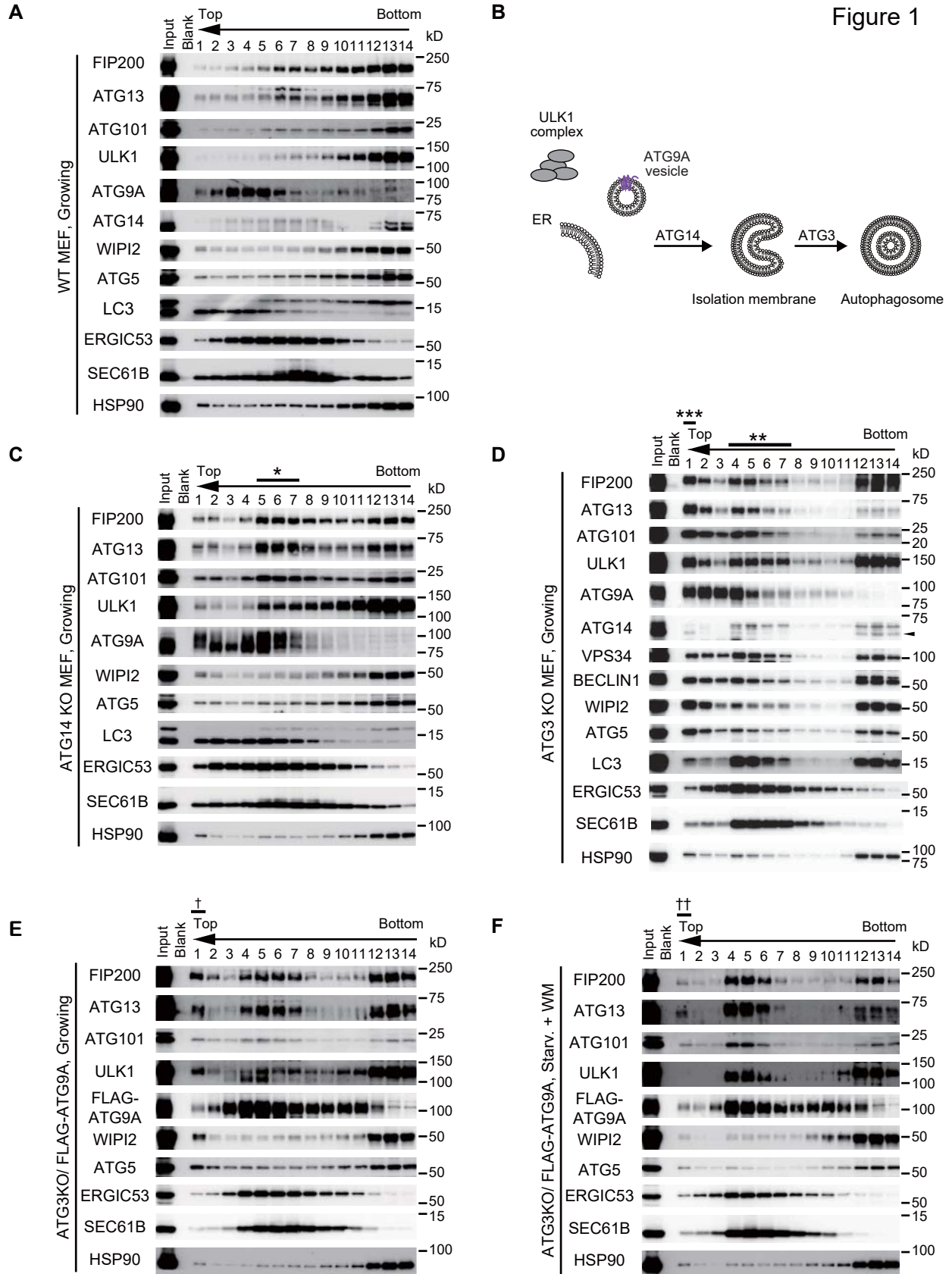
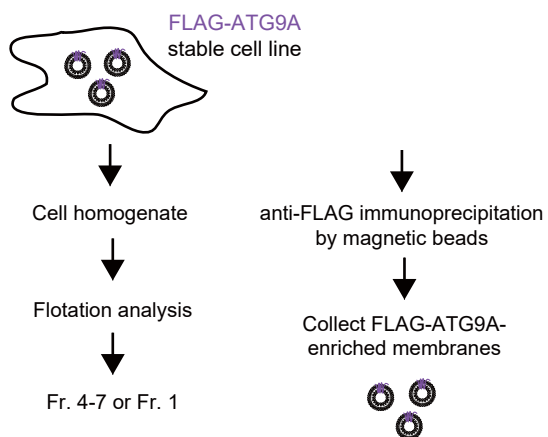
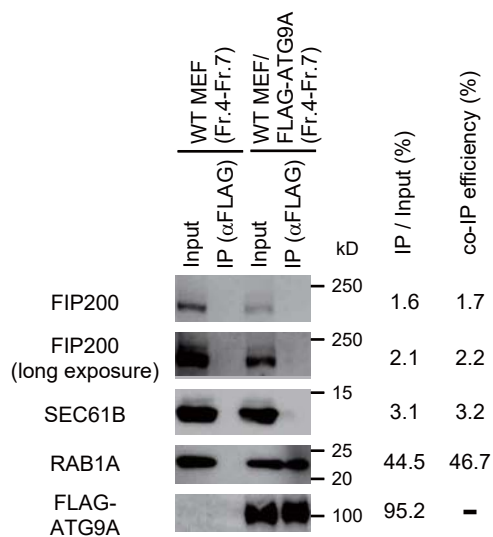


Figure 2

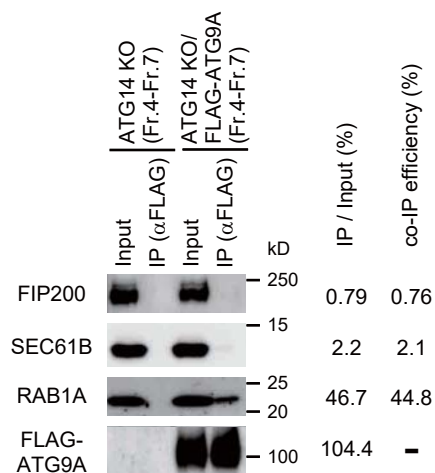
A



B



C



D

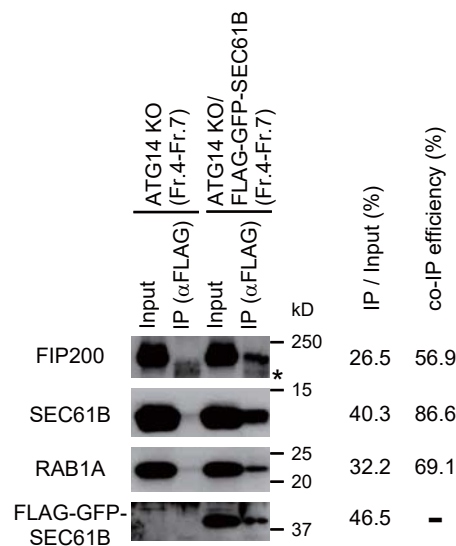
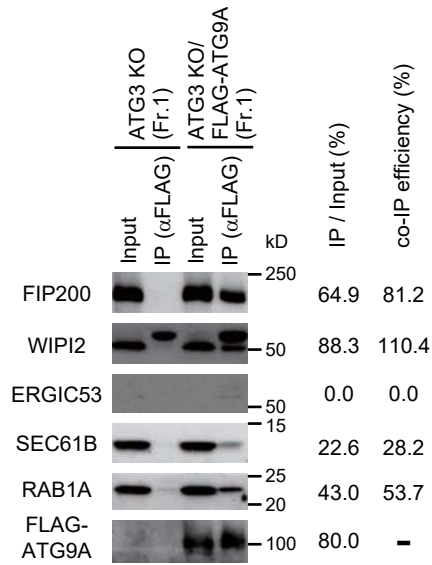
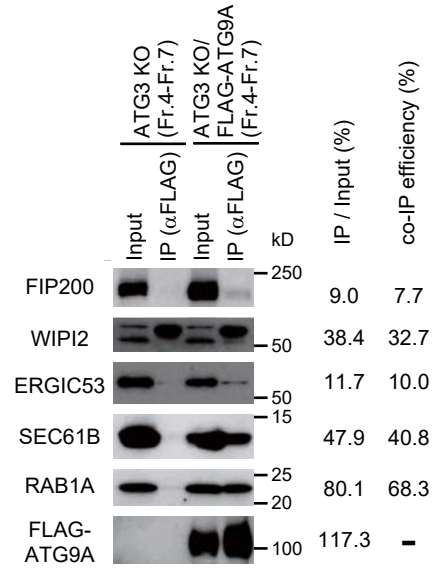


Figure 3

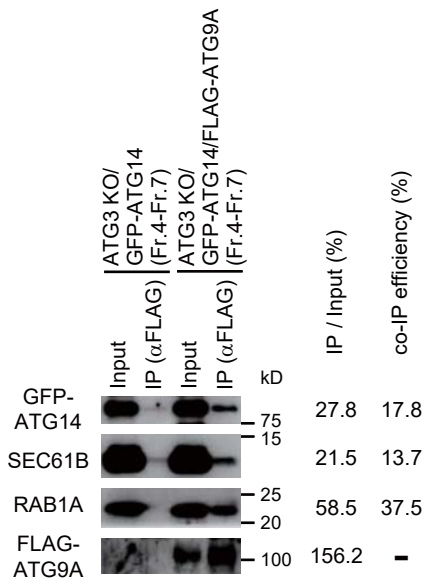
A



B



C



D

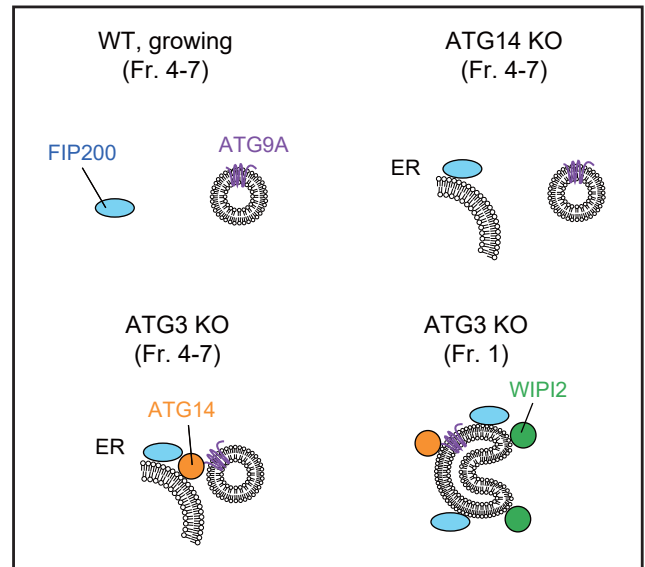
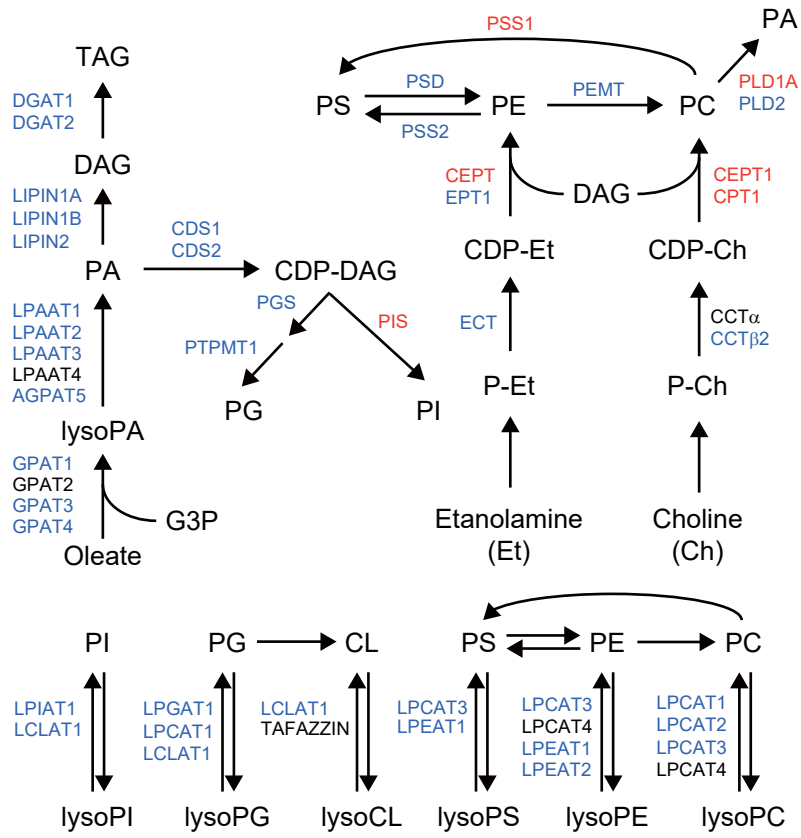


Figure 4

A



B

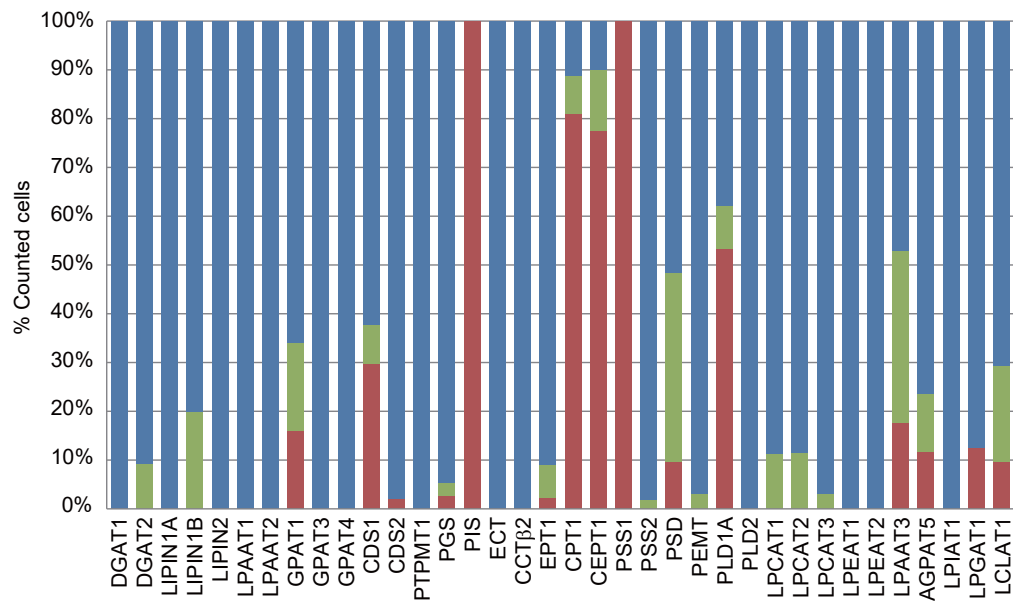
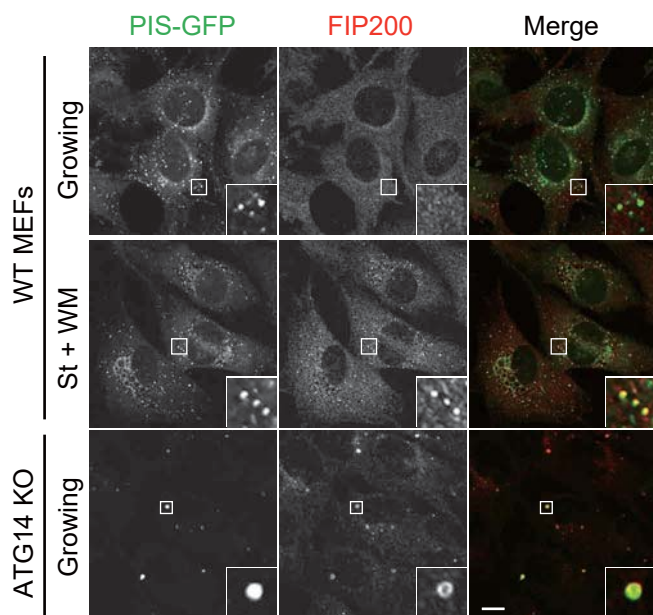
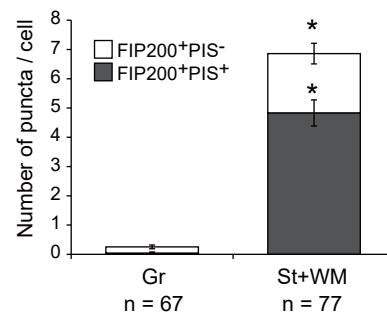


Figure 5

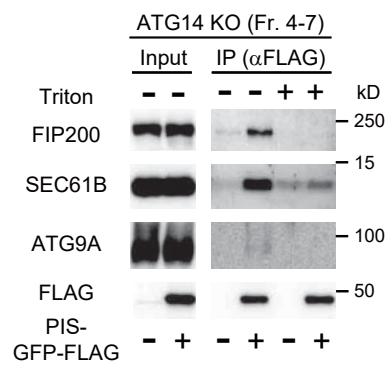
A



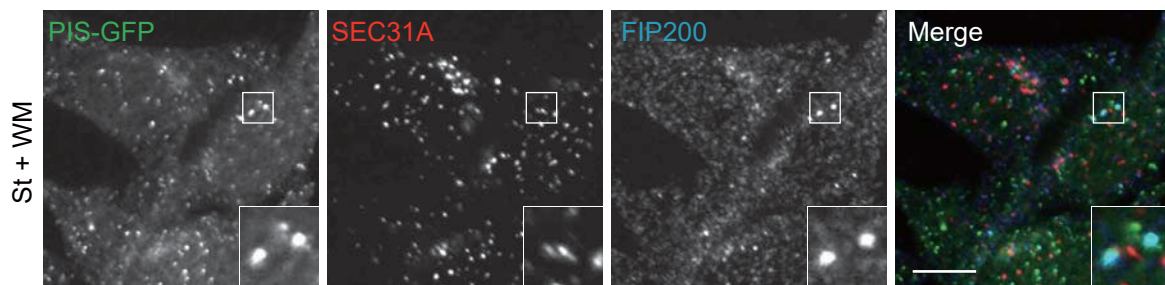
B



E



C



D

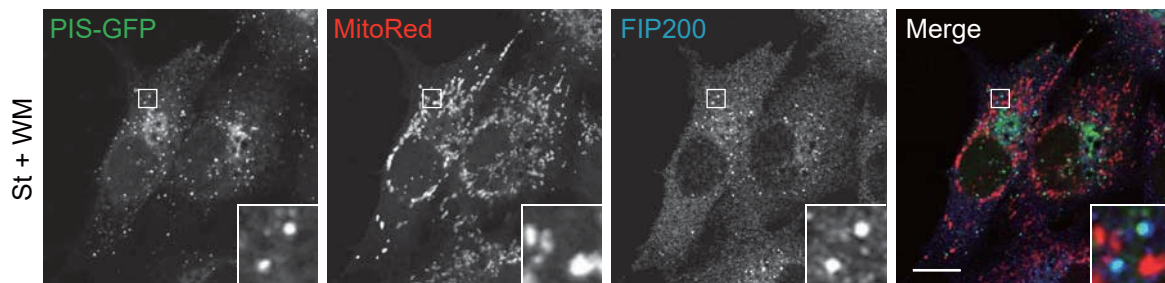


Figure 6

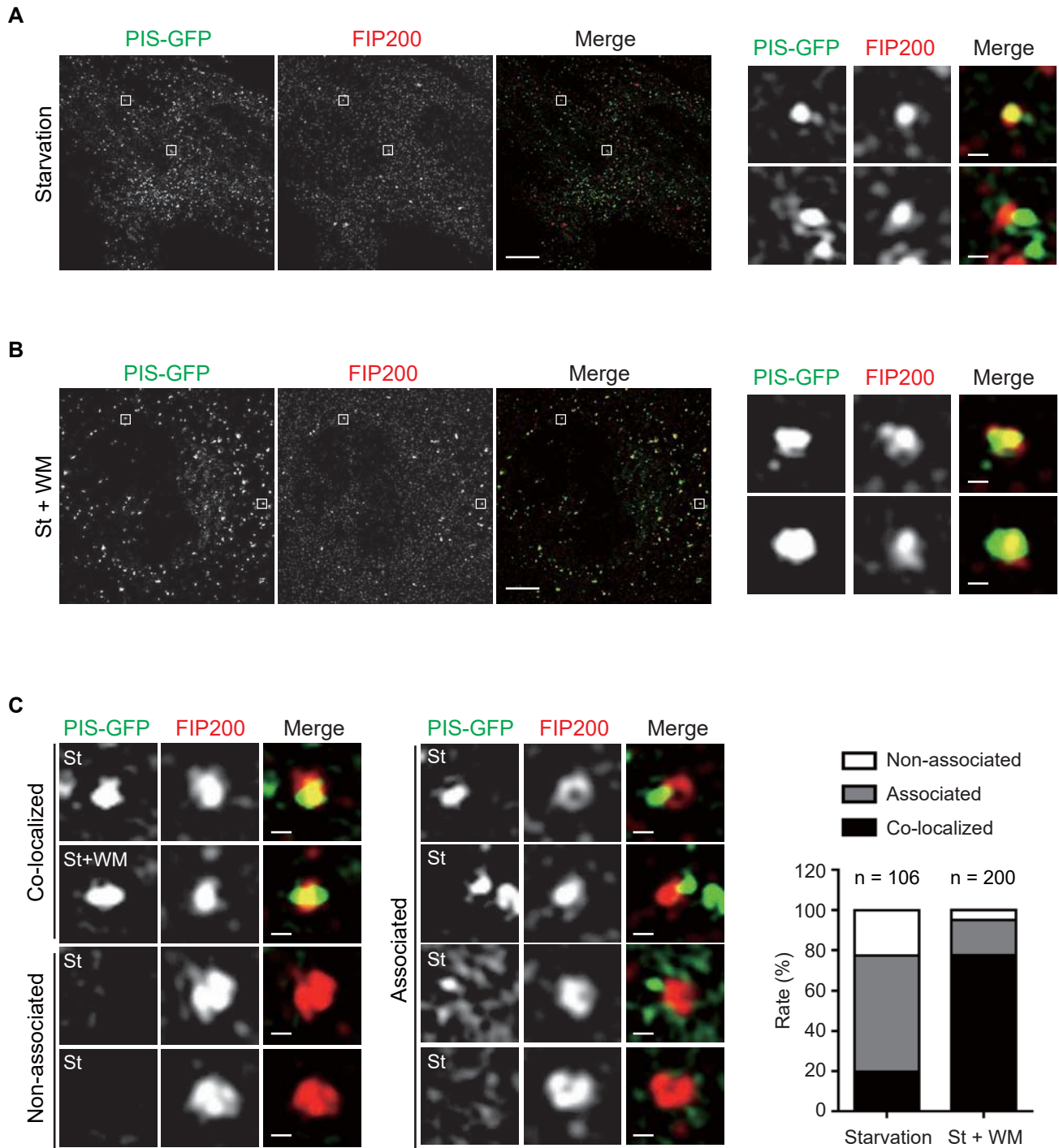
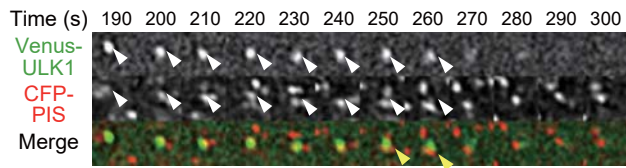
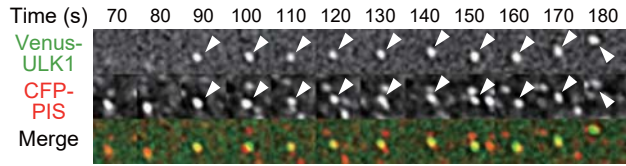
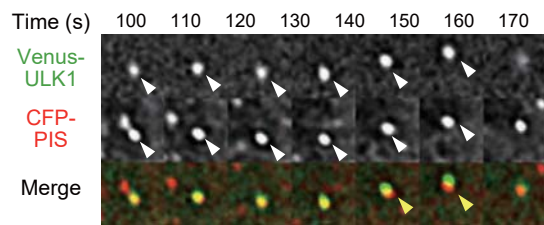
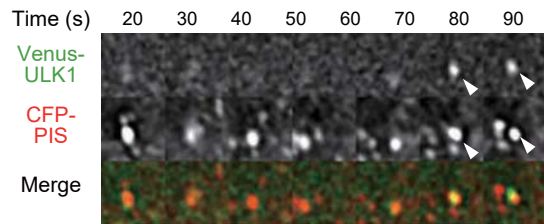


Figure 7

A



B



C

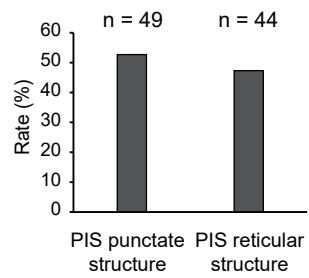


Figure 8

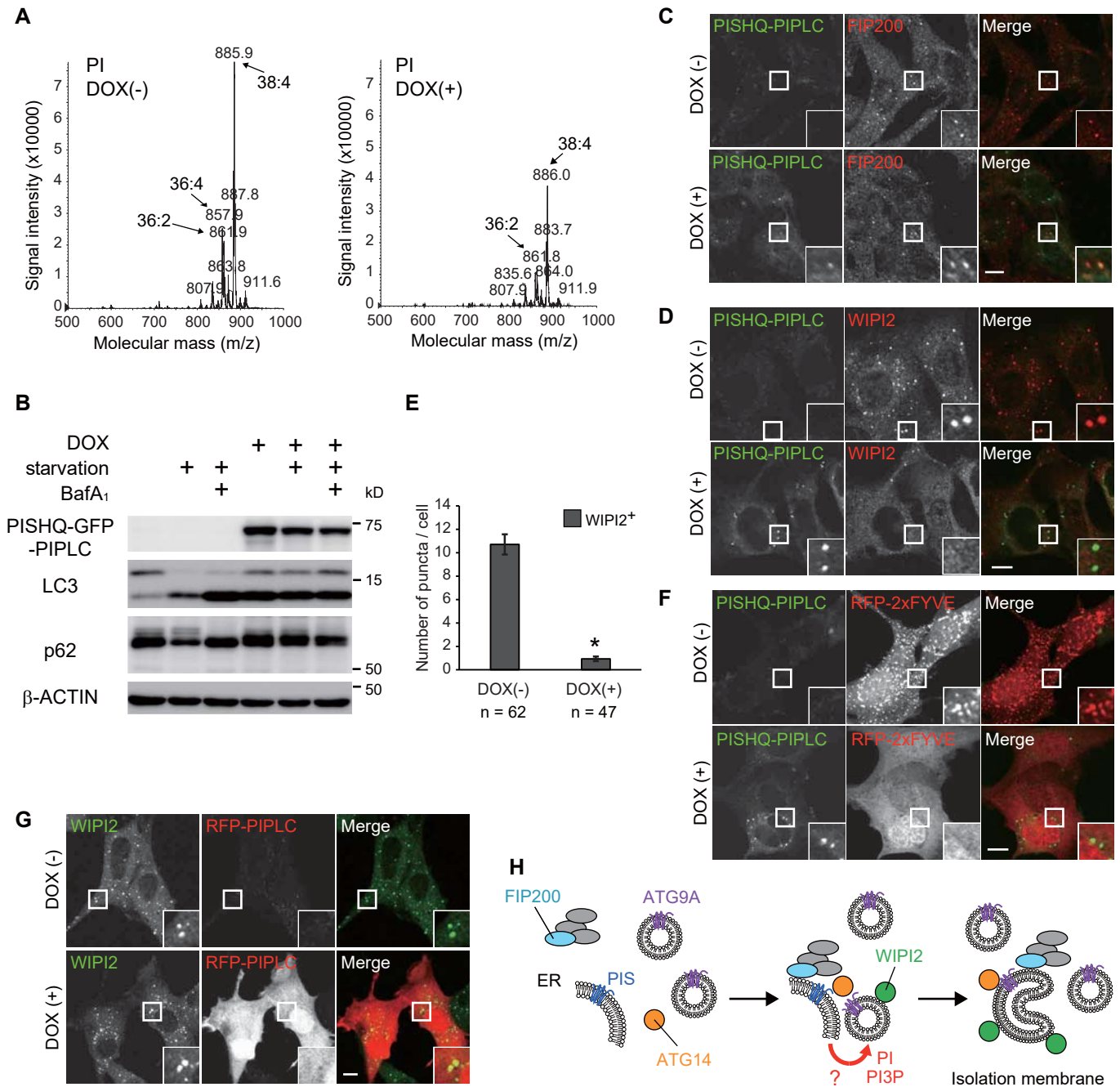


Figure EV1

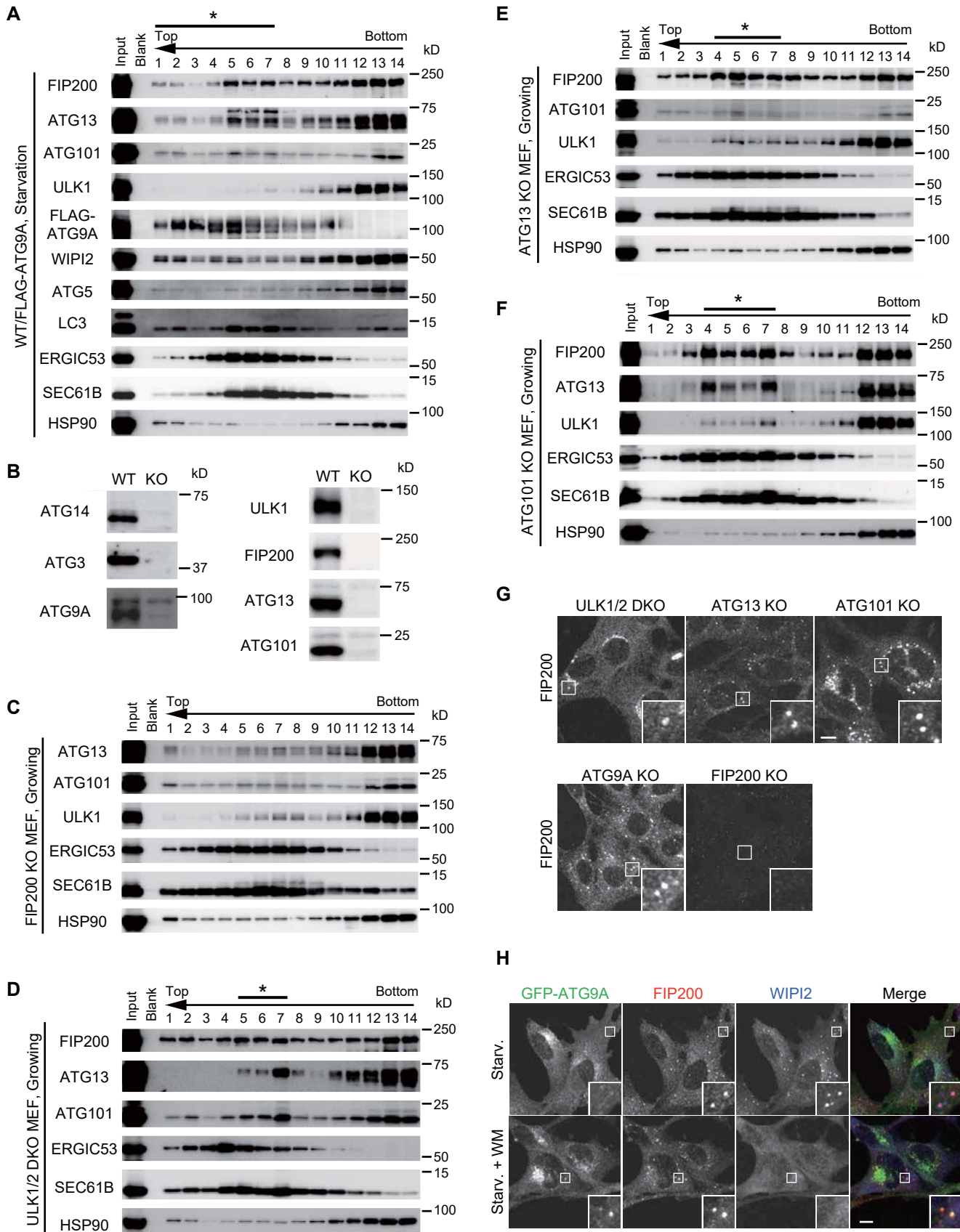


Figure EV2

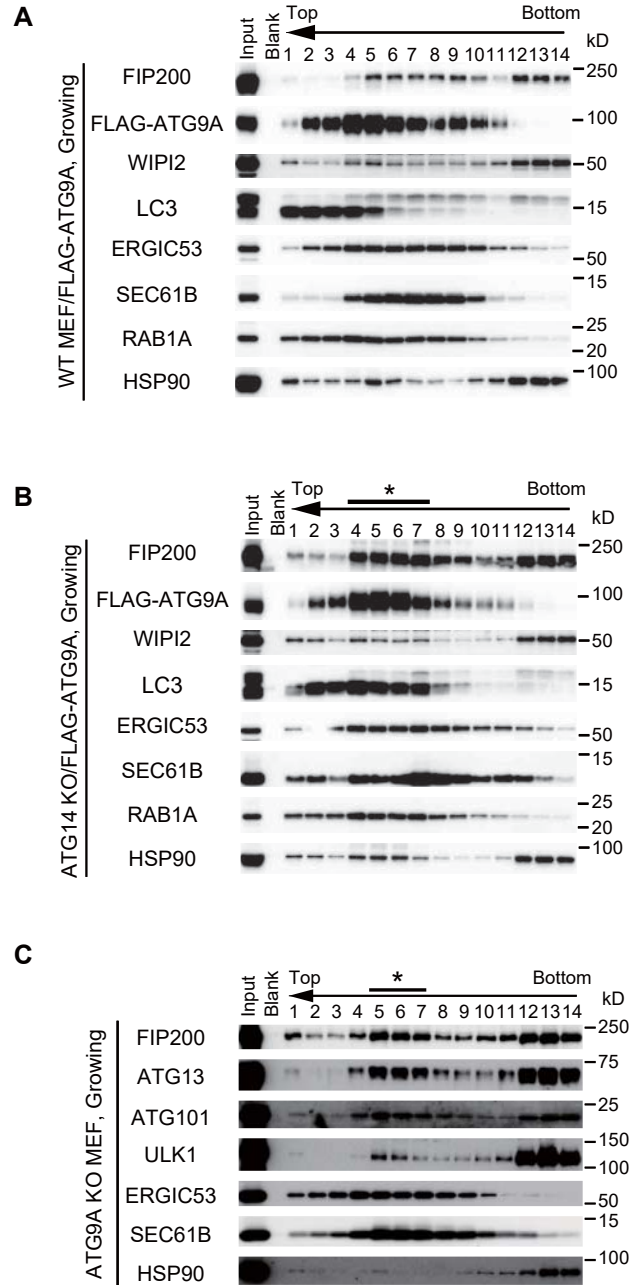


Figure EV4

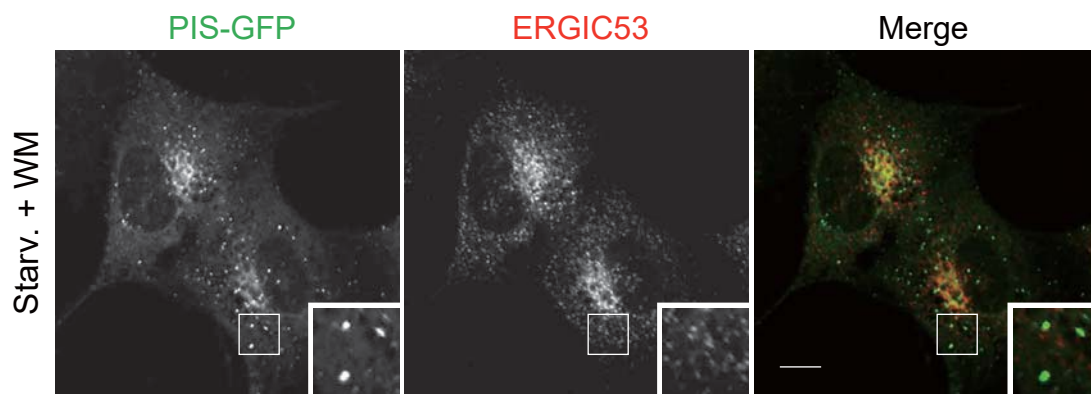


Figure EV5

